Check for updates

The Aβ42:Aβ40 ratio modulates aggregation in beta-amyloid oligomers and drives metabolic changes and cellular dysfunction

Annika Haessler, Stefanie Gier, Nathalie Jung and
Maike Windbergs*

Institute of Pharmaceutical Technology, Goethe University Frankfurt, Frankfurt am Main, Germany

The pathophysiological role of Aβ42 oligomers in the onset of Alzheimer's disease (AD) is heavily disputed, pivoting research toward investigating mixed oligomers composed of Aβ42 and Aβ40, which is more abundant but less aggregation-prone. This study investigates Aβ42:Aβ40 oligomers in different ratios, examining their adverse effects on endothelial cells, neurons, astroglia, and microglia, as well as in a human blood−brain barrier (BBB) model. Combining label-free Raman microscopy with complementary imaging techniques and biochemical assays, we show the prominent impact of Aβ40 on Aβ42 fibrillation, suggesting an inhibitory effect on aggregation. Mixed oligomers, especially with low proportions of Aβ42, were equally detrimental as pure Aβ42 oligomers regarding cell viability, functionality, and metabolism. They also differentially affected lipid droplet metabolism in BBB-associated microglia, indicating distinct pathophysiological responses. Our findings demonstrate the overarching significance of the Aβ42:Aβ40 ratio in Aβ oligomers, challenging the traditional focus on Aβ42 in AD research.

KEYWORDS

Alzheimer's disease, Aβ oligomers, blood−brain barrier, Raman microscopy, lipid droplets, Aβ42:Aβ40

1 Introduction

Alzheimer's disease (AD) is a neurodegenerative disorder characterized by extracellular deposition of aggregated beta-amyloid (Aβ) peptides, so-called Aβ plaques, and buildup of intracellular hyperphosphorylated tau, both triggering neurodegeneration (DeTure and Dickson, 2019). Although Aβ and tau are considered hallmarks, the past decades of research were mainly steered by the amyloid hypothesis, highlighting Aβ aggregation as the cause of AD (Krafft et al., 2022). However, this postulation has been repeatedly challenged since numerous therapeutic approaches focusing on Aβ plaques have not led to a significant improvement in the disease (Zhang et al., 2023). Moreover, Aβ aggregation and plaque formation start years before symptomatic onset, thus, these Aβ-targeting treatments may also simply be too late to effectively cure AD (Zhang et al., 2023). Therefore, the amyloid hypothesis has been revised, identifying soluble Aβ oligomers, rather than Aβ plaques, as the primary toxic amyloid type (Vadukul et al., 2020; Deleanu et al., 2022; Krafft et al., 2022). While ample evidence underlines the harmful effect of Aβ oligomers, therapeutic developments are still inadequate, and thus, their actual toxicity is heavily discussed (Huang and Liu, 2020). So far, small oligomers consisting of the aggregation-prone Aβ42 have been identified as most damaging, while Aβ40 is considered as rather neuroprotective, inhibiting Aβ42 aggregation (Vadukul et al., 2020; Jan et al., 2008). As a result, many *in vitro* studies use only pure Aβ42 oligomers, yet it is doubtful whether this approach emulates the *in vivo* tissue situation, where

Aβ42 is mixed with Aβ isoforms of differing lengths (Deleanu et al., 2022). For instance, N-terminally truncated Aβ isoforms like Aβ4-42 form stable oligomeric aggregates and promote fibril formation whilst being similarly toxic as Aβ42 aggregates (Bouter et al., 2013). These N-terminally truncated isoforms and full-length Aβ species are expressed by various cells in the brain, including neurons, astroglia and oligodendrocytes (Sasmita et al., 2024; Hampel et al., 2021). In inflammatory conditions, such as in AD, the production of Aβ, and especially truncated isoforms, is even more enhanced, thereby aggravating disease progression (Meraz-Ríos et al., 2013; Beretta et al., 2024). Additionally, the inflamed state of microglia, astroglia and oligodendrocytes as well as associated cellular dysfunction fuel amyloid aggregation (Kenigsbuch et al., 2022; Alasmari et al., 2018). Moreover, Aβ40 is much more abundant in the brain compared to Aβ42, highlighting the strong probability of Aβ42 and Aβ40 co-aggregation as one of the earliest pathophysiological changes in the disease (Zoltowska et al., 2016). Various reports have indicated that the Aβ42:Aβ40 ratio determines toxicity, an important circumstance considering the development of new therapeutic antibodies only targeting pure Aβ42 oligomers (Kwak et al., 2020; Kuperstein et al., 2010; Chang and Chen, 2014; Sandberg et al., 2022).

So far, studies investigating the Aβ42:Aβ40 ratio mainly focused on physiochemical properties, and with evaluation of toxicity having been mostly restricted to neurons, toxicity induced by mixed Aβ oligomers may have been overlooked (Chang and Chen, 2014; Deleanu et al., 2022; Jan et al., 2008). Specifically, Aβ oligomers cause or exacerbate various detrimental processes, encompassing mitochondrial dysfunction, lipid dysregulation, (neuro-)inflammation, and blood–brain barrier (BBB) breakdown (Solis et al., 2020; Tarawneh, 2023; Hernandez-Zimbron et al., 2012; Singh, 2022; Zhao et al., 2023). Mitochondrial dysfunction, for instance, arises early in AD, resulting in decreased ATP production and rising levels of reactive oxygen species (Hernandez-Zimbron et al., 2012; Moreira et al., 2010). The associated release of mitochondrial cytochrome into the cytosol is an inducer of apoptosis, amplified by overexpression of cytochrome c (Chandra et al., 2002; Moreira et al., 2010). Glial cells like astroglia and microglia further contribute to neurodegeneration by shifting toward a pro-inflammatory state, elevating cytokine secretion and altering lipid metabolism (de Dios et al., 2023; Franciosi et al., 2005). In this context, lipid droplets have been central to recent research due to their dynamic involvement in cell metabolism (Ralhan et al., 2021; Zhao et al., 2023). Especially cholesterol and unsaturated lipids have been identified as essential contributors to AD, but their exact pathophysiological role remains elusive (Loving and Bruce, 2020). While unusual cholesterol accumulation is generally associated with AD, the impact of unsaturated and saturated lipids is more ambiguous (Loving and Bruce, 2020). For example, unsaturated lipids like anti-inflammatory ω-3 fatty acids contrast polyunsaturated lipids like prostaglandins, which sustain inflammation (Yin, 2023). Another still mostly unexplored function of particularly microglia is the formation of tunneling nanotubes (TNTs), which form bridges between distant cells, allowing for communication and organelle transfer (Wang and Gerdes, 2015). They have also been identified as a transportation system for Aβ, potentially explaining the spread of toxic peptides in the central nervous systems (Dilna et al., 2021; Wang and Gerdes, 2015). In addition, AD-related aberrant angiogenesis has been observed in *in vitro* studies, implying direct damaging effects on endothelial cells (Parodi-Rullán et al., 2020). In 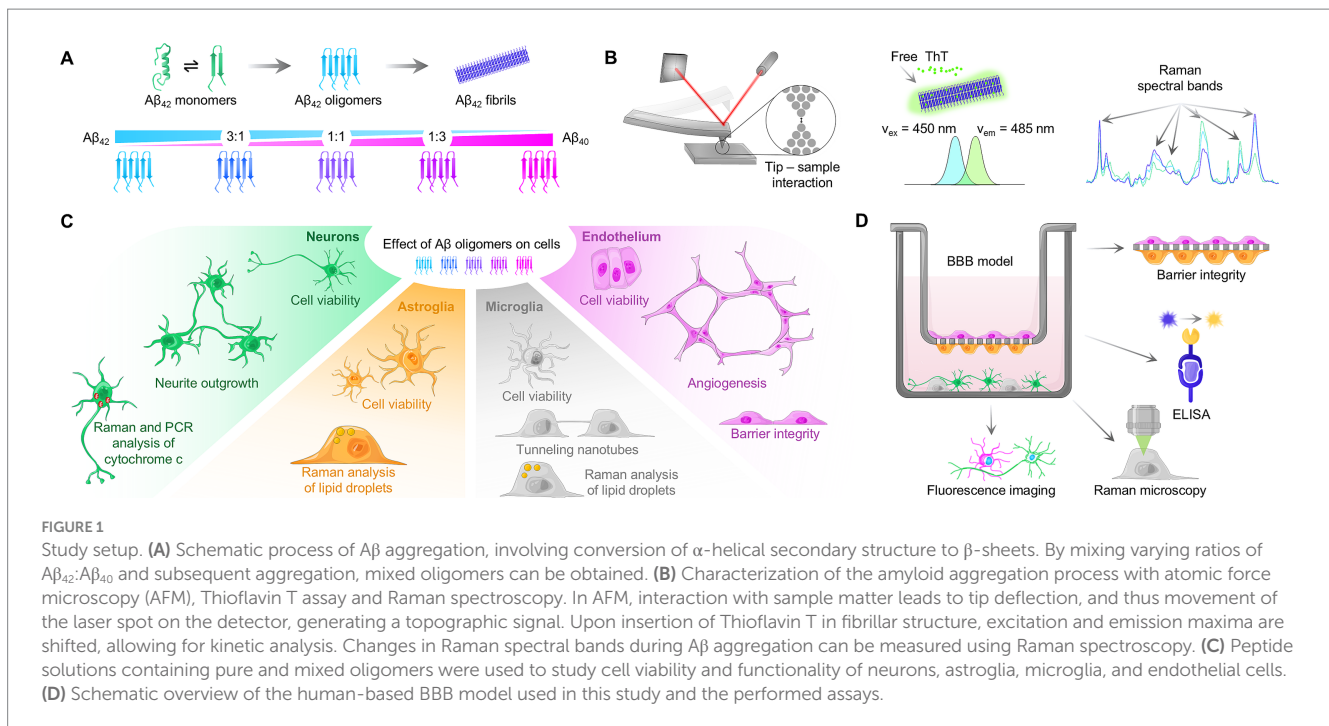a tissue-context, the convergence of these single-cell effects leads to the breakdown of the BBB (Parodi-Rullán et al., 2020; Tarawneh, 2023; Solis et al., 2020). Despite the significant scientific interest in each of these individual mechanisms, they have mainly been studied *in vitro* using pure Aβ42 oligomers, which lack the physiological relevance of oligomers composed of varying Aβ42:Aβ40 ratios.

Quantitative *in vitro* assays are crucial for elucidating such mechanisms, however, obtaining comprehensive biochemical information is equally important. In this regard, confocal Raman microscopy has recently gained traction as a label-free technique, giving simultaneous insight into various biomolecular processes. Based on the inelastic scattering of light, Raman spectra provide specific chemical signatures stemming from the unique combination of bonds in molecules such as desoxyribonucleic acid (DNA), ribonucleic acid (RNA), lipids, or proteins (Jung et al., 2021; Pezzotti, 2021). Confocal Raman microscopy holds a distinct advantage over fluorescence microscopy due to the latter's limited number of fluorescence channels and the requirement of a known target. By scanning cells or tissues, hyperspectral Raman data containing spatially resolved, unbiased biochemical information is obtained, which is especially valuable in elucidating poorly understood molecular changes. Additionally, its sensitivity to molecular conformation makes Raman spectroscopy a valuable tool for studying Aβ aggregation, which involves the conversion of $α$-helical secondary structure to β-sheets (Mallesh et al., 2023). Thus, both Raman imaging and spectroscopy hold great potential for analyzing neurodegeneration but are underutilized due to the complexity of the resulting spectral data, requiring specific expertise.

In this study, we combined the potential of confocal Raman microscopy and spectroscopy with various *in vitro* assays to comprehensively examine the influence of the Aβ42:Aβ40 ratio in oligomers on pathophysiological alterations in cells (Figure 1). State-of-the-art techniques enabled detailed physicochemical characterization, including the Thioflavin T (ThT) assay to study the impact of the Aβ42:Aβ40 ratio on aggregation kinetics, and atomic force microscopy (AFM) combined with Raman spectroscopy to distinguish between different types of Aβ aggregates. Furthermore, we examined the impact of pure and mixed oligomers on cell types critically affected by AD, specifically endothelial cells, neurons, astroglia, and microglia. By conducting an individual analysis for each cell type, we investigated effects on viability, functionality, and metabolism, thereby improving the understanding of Aβ oligomer toxicity. Of particular interest were neuronal dysfunction, differences in the composition of lipid droplets in astroglia and microglia, TNT formation, effects on endothelial barrier integrity, and angiogenesis. Lastly, we examined the effects of selected Aβ oligomers in a human *in vitro* model of the BBB, allowing for cellular interactions in a tissue microenvironment. Overall, our study enabled a detailed assessment of the effects of Aβ42:Aβ40 ratio in oligomers on multiple cell types of the brain by systematically unraveling molecular changes and functional impairment upon Aβ-induced toxicity.

2 Materials and methods

If not stated otherwise, chemicals and cell culture reagents were purchased from Merck KGaA (Darmstadt, Germany) and Thermo Fisher Scientific Inc. (Waltham, United States). Ultrapure water was purified with a PURELAB Flex 2 system (Veolia Water Technologies Deutschland GmbH, Celle, Germany).

FIGURE 1
Study setup. **(A)** Schematic process of Aβ aggregation, involving conversion of α-helical secondary structure to β-sheets. By mixing varying ratios of Aβ$_{42}$:Aβ$_{40}$ and subsequent aggregation, mixed oligomers can be obtained. **(B)** Characterization of the amyloid aggregation process with atomic force microscopy (AFM), Thioflavin T assay and Raman spectroscopy. In AFM, interaction with sample matter leads to tip deflection, and thus movement of the laser spot on the detector, generating a topographic signal. Upon insertion of Thioflavin T in fibrillar structure, excitation and emission maxima are shifted, allowing for kinetic analysis. Changes in Raman spectral bands during Aβ aggregation can be measured using Raman spectroscopy. **(C)** Peptide solutions containing pure and mixed oligomers were used to study cell viability and functionality of neurons, astroglia, microglia, and endothelial cells. **(D)** Schematic overview of the human-based BBB model used in this study and the performed assays.

2.1 Aβ preparation

Aβ$_{42}$ or Aβ$_{40}$ peptide (Kaneka Eurogentec S.A., Seraing, Belgium) was dissolved in hexafluoroisopropanol (HFIP, Th. Geyer GmbH & Co. KG, Renningen, Germany) and incubated for 2 h at room temperature. Then, peptides were optionally mixed to ratios of Aβ$_{42}$:Aβ$_{40}$ of 3:1 (Aβ$_{3:1}$), 1:1 (Aβ$_{1:1}$), and 1:3 (Aβ$_{1:3}$) and aliquoted in Eppendorf tubes. HFIP was evaporated overnight in a vacuum, and the dry peptide films were stored at −70°C until use.

2.2 Thioflavin T fluorescence assays

Dried peptide films (Pure Aβ$_{42}$, Aβ$_{3:1}$, Aβ$_{1:1}$, Aβ$_{1:3}$ and pure Aβ$_{40}$) were dissolved in 50 mM sodium hydroxide to a 45.5 µM solution and bath sonicated for 5 min. Next, peptide solutions were diluted to 20 µM in black 96-well plates using 60 mM HCl and supplemented with 20 µM Thioflavin T (ThT, Biomol GmbH, Hamburg, Germany). For the vehicle control, the same procedure was repeated but without peptide. The assay was performed using a TECAN Spark plate reader and a humidity cassette (TECAN Group AG, Männedorf, Switzerland) for 6 h at 37°C with excitation at 448 ± 7 nm and emission at 485 ± 20 nm, measuring every 5 min. For data analysis of each experimental run, the intensity of the vehicle control was subtracted from the intensities recorded for the different peptide ratios.

2.3 Aβ aggregation

Peptide aggregation protocols were adapted from the protocol by Stine et al. (2011). Briefly, monomeric Aβ$_{42}$ was prepared by dissolving dried peptide film in cold 0.02% ammonia for 10 min

on ice and adding ice-cold sterile ultrapure water to a final concentration of 100 µM. Oligomers of Aβ$_{42}$ (OAβ$_{42}$), Aβ$_{1:1}$ (OAβ$_{1:1}$), and Aβ$_{3:1}$ (OAβ$_{3:1}$) were obtained by initially dissolving peptide in 0.02% ammonia, followed by sterile ultrapure water and incubation at 4°C overnight. Fibrils of Aβ$_{42}$ (FAβ$_{42}$), oligomers of Aβ$_{40}$ (OAβ$_{40}$), and Aβ$_{1:3}$ (OAβ$_{1:3}$) were obtained by adding sterile 10 mM HCl and incubating at 37°C overnight instead. All peptide solutions and aggregates were freshly prepared for each experiment.

2.4 Atomic force microscopy

Atomic force microscopy (AFM) was performed on a JPK Nanowizard III (Bruker Corporation, Billerica, United States) using ACTA tips (APPNano, Mountain View, United States) with the following properties: tip-radius < 10 nm, spring constant 37 N/m, frequency 300 kHz, 125 µm length, 30 µm width, 4 µm thickness, and an aluminum cantilever coating. Samples were prepared as follows: cleaned mica sheets were glued to microscopy slides using epoxy glue and dried overnight. Then, they were transferred to a laminar-air-flow bench and washed using 300 µL of 96% ethanol (VWR International GmbH, Darmstadt, Germany), and left to dry inside the bench. Mica was cleaved using tape strips for 2–4× until a smooth surface free from cracks was visible. Next, freshly prepared peptide solutions were diluted using ultrapure water to a concentration of 20 µM (monomers, oligomers) or 5 µM (fibrils). Samples were immediately spotted on the mica and incubated for 10 min. Using 100 µL of filtered (0.22 µm) ultrapure water, excess sample solution was washed off. Afterward, samples were placed in a vacuum and stored for a maximum of 16 h before AFM imaging.

2.5 Drop-coating deposition Raman spectroscopy (DCDRS), spectral processing, cross-correlation analysis and peak ratio analysis

Ten microliters drops of peptide solution were placed on calcium fluoride dishes (Korth Kristalle GmbH, Altenholz, Germany) and dried for 30 min in a fume hood. Raman spectra at 30 randomly chosen positions in the middle of the dried drop were acquired with a confocal Raman microscope alpha300R (WITec GmbH, Ulm, Germany) equipped with a 50x objective (NA 0.8) and a 532 m laser set to a power of 20 mW in front of the objective. Integration time was set to 2–8 s. Background and cosmic rays were removed using the ProjectFour software (WITec GmbH, Ulm, Germany). Preprocessed spectra were then imported to Matlab (The Mathworks Inc., Natick, United States). Using the spectra of $A\beta_{42}$ monomers, oligomers, and fibrils, a cross-correlation analysis was performed to investigate which Raman peaks are subject to sequential change (Lasch and Noda, 2019). With this knowledge, specific peak ratios (1,240 cm^{-1}/1307 cm^{-1}, 1,671 cm^{-1}/1447 cm^{-1}, 1,671 cm^{-1}/1555 cm^{-1}, 1,671 cm^{-1}/1609 cm^{-1}, and 2,935 cm^{-1}/2850 cm^{-1}) were chosen for peak ratio analysis according to the assignments in Supplementary Table S1.

2.6 General cell culture

Human SH-SY5Y neuroblastoma cells (Cell lines services, Eppelheim, Germany) were cultured in DMEM with 10% fetal calf serum (FCS) and used up for up to 8 passages (maximum passage 12). Human CCF-STTG1 astroglia (ATCC, Manassas, United States) were cultured in RPMI with 10% FCS and used up for up to 10 passages (maximum passage 12). Human HMC3 microglia (ATCC, Manassas, USA) were cultured in a-MEM with 10% FCS and used for up to 10 passages (maximum passage 12). The human cerebral microvascular endothelial cell line hCMEC/D3 (Cedarlane Labs, Burlington, United States) was cultured on collagen-coated flasks (10 $\mu g/cm^2$) in EGM-2 medium (Promocell, Heidelberg, Germany) used for up to 6 passages (maximum passage 34). Cells were passaged by trypsinization every 7 days. hCMEC/D3 endothelial cells were used for assays at 30,000 $cells/cm^2$, differentiated SH-SY5Y at 45,000 $cell/cm^2$, HMC3 microglia and CCF-STGG1 astroglia at 24,000 $cells/cm^2$, if not stated otherwise.

2.7 Immunofluorescence staining and imaging

All fluorescence staining followed a standardized procedure: after fixation, cells were washed 3× in PBS + 0.05% Tween 20 (PBS-T) for 5 min and permeabilized with 0.2% Triton-X for 5 min. Samples were washed again 3x in PBS-T for 5 min. For antibody staining, samples were first blocked in 5% goat serum and 5% BSA for 20 min. Then, without washing, primary antibody (1:1000 β-III tubulin mouse-anti-human, Thermo Fisher Scientific, Waltham, United States) in blocking buffer (5% bovine serum albumin +5% goat serum in PBS) was added and incubated under gentle shaking at 4°C overnight. Samples were washed 3× in PBS-T for 5 min, and secondary antibody in PBS (1:400 Alexa Fluor 633 goat-anti-mouse) was added and incubated under

gentle shaking for 1 h at room temperature. Subsequently, samples were washed 3x with PBS-T for 5 min. For actin staining, samples were incubated after permeabilization and washing with Alexa Fluor 488 Phalloidin or Alexa Fluor 555 Phalloidin under shaking conditions for 1 h at room temperature. Then, samples were washed 3× in PBS-T for 5 min. After the respective staining (antibody or phalloidin or a combination) and washing, samples were counterstained with DAPI (1:100) in PBS under shaking for 5 min at room temperature. After washing 2× in PBS-T and 1x in ultrapure water for 5 min each, samples were mounted in FluorSave (Merck KGaA, Darmstadt, Germany) and dried overnight. Samples were stored at 4°C. Imaging was performed using an inverted confocal laser scanning microscope equipped with 10× (NA 0.45), 20× (NA 0.8), and 40× oil immersion (NA 1.4) objectives (Zeiss, Oberkochen, Germany).

2.8 SH-SY5Y cell differentiation

SH-SY5Y neuroblastoma cell differentiation protocols were adapted from existing literature using retinoic acid and brain-derived neurotrophic factor (BDNF), which generates an excitatory neuronal population with glutamatergic and cholinergic markers (Encinas et al., 2000; Dravid et al., 2021; Shipley et al., 2016; Targett et al., 2024). Briefly, SH-SY5Y cells were seeded in T-75 flasks at 10,000 $cells/cm^2$ in DMEM supplemented with 10% FCS and left to adhere overnight. On day 1 post seeding, medium was changed to DMEM supplemented with 2.5% FCS, 2 mM glutamine and 10 µM retinoic acid. On day 4 post seeding, medium was changed to Neurobasal™ medium enriched with 50 ng/mL BDNF, 1x B-27(TM) supplement, and 10 µM retinoic acid. On day 7 post seeding, cells were gently passaged, counted, and seeded for experimental use. To verify differentiation, fluorescence staining of β-III tubulin was performed according to the protocol above (Supplementary Figure S2).

2.9 Viability assay

The respective cells were seeded in flat-bottom 96-well plates and incubated overnight. The next day, cells were treated with pure and mixed oligomers at 10, 5, 2.5, 1.25, and 0.6125 µM, medium (control), or PBS. Treatment with 100 ng/mL LPS + 20 ng/mL IFN-y (Immunotools GmbH, Friesoythe, Germany) was included for HMC3 microglia. After 24 h, medium was discarded, and fresh medium supplemented with 1 mg/mL 3-(4,5-dimethylthiazol-2-yl)-2,5-diphenyltetrazolium bromide (MTT) reagent was added and incubated for 4 h at 37°C. Then, medium was discarded again, 100 µL of DMSO was added per well, and the plate was placed on a lab shaker for 15 min. After ensuring the formazan crystals had dissolved, the absorption was measured at 570 nm in a TECAN Spark plate reader (TECAN Group AG, Männedorf, Switzerland). For data evaluation, viability was normalized to the control.

2.10 Neurite outgrowth assay

To further verify the differentiation of SH-SY5Y cells, neurite outgrowth was compared between SH-SY5Y neuroblastoma cells and differentiated SH-SY5Y neurons. Briefly, cells were seeded in a 24-well

plate left to settle for 24 h. The next day, phase contrast images were acquired using an inverted Leica DMi8 microscope (LEICA microsystems, Wetzlar, Germany) equipped with a 20x objective. Images were then imported to Fiji, converted to 8-bit images and neurite length was measured using the NeuronJ plugin (Meijering et al., 2004; Schindelin et al., 2012). For the investigation of the toxicity of pure and mixed Aβ oligomers, differentiated cells were seeded in 24-well plates in Neurobasal™ medium enriched with 1x B-27(TM) supplement and treated with 10 µM of the respective peptide solution or medium (control) for 24 h. Neurite length was measured as described above.

2.11 PCR analysis of cytochrome c messenger RNA levels

Briefly, differentiated SH-SY5Y cells were seeded in a 24-well plate and incubated for 24 h, followed by 24 h treatment with 10 µM $OAβ_{42}$, $OAβ_{1:3}$, or medium. Cells were lyzed via the addition of 350 µL TRIzol™ per well, and total RNA was isolated using the Direct-zol RNA MiniPrep Plus Kit (Zymo Research Europe GmbH, Freiburg, Germany) according to the manufacturer; concentration as well as purity were validated photometrically in a TECAN Spark plate reader using the NanoQuant Plate (TECAN Group AG, Männedorf, Switzerland). First-strand synthesis was performed with the Maxima H Minus cDNA Synthesis Master Mix Kit (Thermo Fisher Scientific, Waltham, MA, United States), implementing 250 ng total RNA and following the protocol provided by the manufacturer. Afterward, complementary desoxyribonucleic acid (cDNA) concentration was measured as mentioned above. Cytochrome c (CYC1) messenger RNA (mRNA) level were analyzed via the StepOnePlus Real-Time PCR System (Applied Biosystem, Waltham, MA, United States) using the SYBR Green PowerTrack Master Mix (Thermo Fisher Scientific, Waltham, MA, United States) and 10 ng cDNA. Resulting Ct values were evaluated according to the $2^{-\Delta\Delta Ct}$ method employing glyceraldehyde-3-phosphate dehydrogenase (GAPDH) as a housekeeping gene. Data were subsequently normalized to the untreated control (Livak and Schmittgen, 2001). The following primer pairs (5′–3′ orientation) were used for amplification: GAPDH *forward*: CGGGAAGCTTGTCATCAATGG, GAPDH *reverse*: GGCAGTGAT GGCATGGACTG, CYC1 *forward*: CGGAGGTGGAGGTTCAAGAC, and CYC1 *reverse*: TAGAGACCTTCCCGCAGTGA. Primer efficiency was routinely validated before the experiment.

2.12 Confocal Raman microscopy of cells

The respective cells were seeded on calcium fluoride dishes (Korth Kristalle GmbH, Altenholz, Germany) and incubated overnight. The next day, cells were treated with peptide solutions at 10 µM or medium (control) and incubated for 24 h. Then, cells were fixed in 4% formaldehyde (in PBS) for 10 min, and subsequently washed 3x in PBS. Using a confocal Raman microscope (WITec GmbH, Ulm, Germany) equipped with a 532 nm laser set to a power of 37 mW and a 63× water dipping objective, Raman scans were acquired with an integration time of 0.2 s and a spatial resolution of 500 nm. Background of scans was subtracted using the ProjectFOUR software (WITec GmbH, Ulm, Germany). Scans were then imported to Matlab

(The Mathworks Inc., Natick, United States) to remove cosmic rays, smooth the data (Savitzky–Golay filter, window size 9, order 3), and normalized using the Stand Normal Variate method. Next, data was analyzed using the endmember analysis algorithm N-FINDR (Winter, 1999). Briefly, the number of endmembers in the hyperspectral data set was estimated using the noise-whitened Harsanyi-Farrand-Chang (NWHFC) method. End-member spectra were identified by the N-FINDR algorithm and used to calculate end-member abundance maps. Individual abundance maps were overlayed using Fiji. Spectra were plotted, and peak ratio analysis (refer to detailed peak assignment in Supplementary Table S1) was conducted for cytochrome c and/or lipids. Raman imaging was divided into a pre-study to assess feasibility and a subsequent study which encompassed Raman spectra from 3 to 8 cells in total.

2.13 Tunneling nanotube quantification

Tunneling nanotube (TNT) measurement was adapted from existing protocols (Chakraborty et al., 2023; Kretschmer et al., 2019). Briefly, HMC3 microglial cells were seeded on high-precision glass coverslips (170 ± 5 µm) and incubated overnight. The next day, cells were treated with 10 µM peptide solution or medium (control) and incubated for 24 h. HMC3 cells were then fixed using a two-step fixation protocol: 15 min with 2% formaldehyde and 0.05% glutaraldehyde (Carl Roth GmbH + Co. KG, Karlsruhe, Germany) in PBS, followed by 15 min in 4% formaldehyde in PBS. Subsequently, phalloidin and DAPI staining were performed according to the protocol above, and glass slips were mounted in FluorSave (Merck KGaA, Darmstadt, Germany). Z-stacks were acquired using an inverted confocal laser scanning microscope (LSM900, Carl Zeiss AG, Oberkochen, Germany) using a 20× objective and 0.5 µm step size. For each n and treatment group, 3 z-stacks were acquired at random locations in the sample. Stack scans were then imported to ICY Bioimage analysis software, and TNTs were counted using the TNT annotation tool. A TNT was only counted if the cellular structure hovered above ground level (assessed via z-stack-based spatial resolution of the acquired fluorescence images), if its length exceeded 5 µm, and if its thickness was below 1 µm (Thayanithy et al., 2017; Matejka and Reindl, 2019).

2.14 Transepithelial electrical resistance (TEER) measurement

hCMEC/D3 endothelial cells were seeded at 40,000 cells/cm² on 24-well PET 0.4 µm pore inserts (Brand GmbH + Co KG, Wertheim, Germany) in EGM-2 medium (Promocell, Heidelberg, Germany) without VEGF (vascular endothelial growth factor), supplemented with 50 µg/mL ascorbic acid and 1.4 µM hydrocortisone (Caesar & Loretz GmbH, Hilden, Germany). TEER was measured daily using an the Millicell® ERS-2 (Merck KGaA, Darmstadt Germany) equipped with an EVOM2 electrode (World precision instruments, Sarasota, United States). Plateau TEER was reached on day 3 post seeding, at which point cells were treated with peptide solutions at 10 µM or medium (control) and incubated for 24 h, followed by a final TEER measurement. This experiment was performed in quadruplicate.

2.15 Angiogenesis assay

The angiogenesis assay was adapted from existing literature (Thomas et al., 2017; Faulkner et al., 2014). Briefly, hCMEC/D3 endothelial cells were starved in DMEM without FCS overnight. Geltrex™ (Thermo Fisher Scientific, Waltham, United States) was thawed at 4°C on ice overnight. The next day, a flat-bottom 96-well plate and 10 μL pipette tips were pre-cooled at −20°C for 30 min, and 2.5 μL of Geltrex™ was pipetted into each well. The plate was then placed at 37°C for 30 min. Meanwhile, hCMEC/D3 cells were passaged and counted. After incubation of Geltrex™ in the plate, hCMEC/D3 cells were seeded in EGM-2 basal medium (Promocell, Heidelberg, Germany). After 4 h, cells were treated with peptide solutions at 10 μM, medium (control), or vascular endothelial growth factor (VEGF, positive control). After 20 h, cells were fixed in 4% formaldehyde (in PBS) for 10 min. Phalloidin staining, followed by DAPI staining, was performed according to the protocol above. Fluorescence images for quantitative analysis were acquired using an inverted Leica DMi8 microscope (LEICA microsystems, Wetzlar, Germany) equipped with a 5× objective. Angiogenesis was assessed using the REAVER script in Matlab (The Mathworks Inc., Natick, United States) with standard settings except for a gray threshold of 0.05, averaging filter size of 500, minimum connected component area of 100, and vessel thickness threshold of 3 (Corliss et al., 2020).

2.16 Blood−brain barrier model cultivation

On day 1, 40,000 CCF-STTG1 astroglia were seeded in RPMI +10% FCS on collagen-coated (0.9 mg/mL collagen, 15 μL) basal sides of 24-well inserts (Falcon® cell culture inserts, 0.4 μm pore size, Corning Inc., Corning, United States) and left to attach overnight. On day 2, hCMEC/D3 endothelial cells (50,000 cells) were seeded on the apical side of the insert membrane in EGM-2. HMC3 microglia (5,000 cells) and differentiated SH-SY5Y neurons (45,000 cells) were seeded in the basal compartment on collagen-coated coverslips (0.1 mg/mL, 900 μL, Corning Inc., Corning, United States) in a-MEM + 10% FCS. On day 3, the medium was exchanged for a-MEM + 2% FCS. After initial TEER measurement on day 4, the basolateral compartment was supplemented with 10 μm $A\beta_{42}$, $A\beta_{1:3}$, 100 ng/mL LPS + 20 ng/mL IFN-γ or medium/PBS (control), respectively, and cells were cultivated for additional 24 h.

2.17 Blood−brain barrier model analysis

TEER was measured on day 5 after 24 h incubation with the respective treatment. TEER measurement was performed in quadruplicate. The medium of the basal compartment was collected for enzyme-linked-immunosorbent-assay (ELISA). Briefly, 800 μL of medium was collected per well and centrifuged at 14,000 rpm for 15 min at 4°C to remove cell debris. The supernatant was frozen at −70°C and thawed 1 h prior to analysis. ELISAs of IL-6 and IL-8 were performed according to the manufacturer's instructions (Thermo Fisher Scientific, Waltham, United States). For fluorescence imaging and Raman microscopy, cells were fixed according to the TNT cell fixation protocol above or with 4% formaldehyde (in PBS) for 10 min, respectively. Raman microscopy was performed in duplicate.

Antibody and phalloidin staining were conducted according to the protocol above on cells fixed with the TNT fixation protocol.

2.18 Statistical analysis

Results are shown as mean values ± standard deviation indicated by error bars. Each experiment included technical triplicates and was performed in triplicate if not stated otherwise. Statistical analysis was performed for the following experiments using the specified test. ANOVA followed by Dunnett *post hoc* test: DCDRS peak ratio analysis, viability assay, neurite outgrowth assay, PCR analysis of cytochrome c mRNA levels, tunneling nanotube quantification, angiogenesis assay, IL-6 and IL-8 secretion in the BBB model; student's paired *t*-test: TEER measurements on endothelial cell monocultures, TEER measurements in the BBB model; two sample *t*-test: neurite outgrowth of differentiated neurons. Statistical significance is indicated by $*p < 0.05$, $**p < 0.01$, and $***p < 0.001$ in the figures. If a statistical test was performed, but no significance is indicated, the test was non-significant.
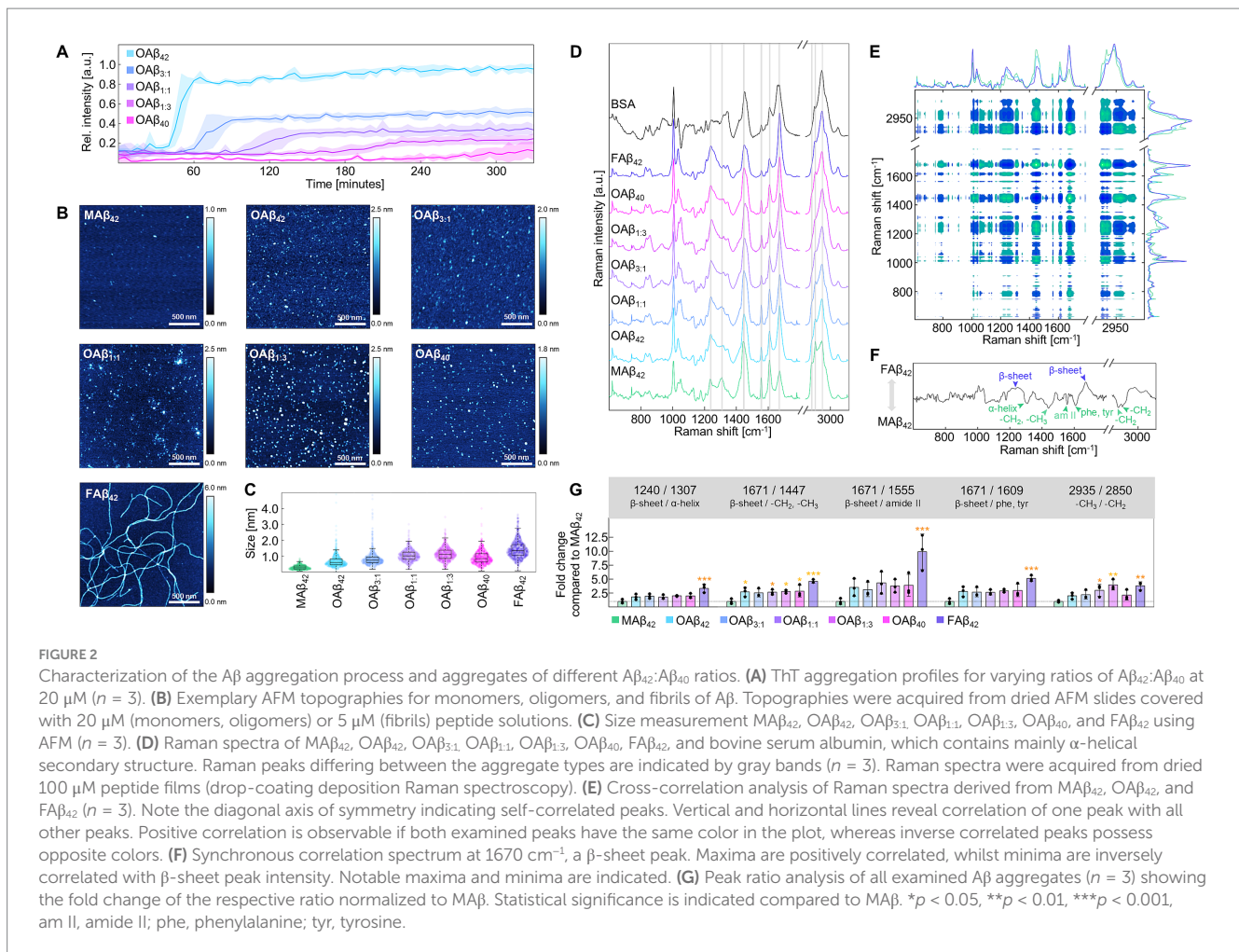
3 Results

3.1 Characterization of the Aβ aggregation process and individual Aβ aggregates

We first investigated the aggregation kinetics of pure and mixed monomeric $A\beta_{42}$ and $A\beta_{40}$ in differing ratios by performing a Thioflavin T (ThT) assay, revealing gradual differences in aggregation curves (Figure 2A). While the $A\beta_{40}$ profile did not reach a plateau in the examined time interval, $A\beta_{42}$ attained a steady state at 0.87 ± 0.07 a.u. after 65 min. The mixed amyloid curves were distributed between the profiles of pure $A\beta_{42}$ and $A\beta_{40}$, differing in steepness of the sigmoid profile and height of the fluorescence plateau. Specifically, profiles of $A\beta_{42}$:$A\beta_{40}$ mixtures with a ratio of 3:1 ($A\beta_{3:1}$), equal mixtures of both species ($A\beta_{1:1}$) and the combination of both species in a 1:3 ratio ($A\beta_{1:3}$) reached their plateau after 110 min at 0.45 ± 0.02 a.u, 155 min at 0.31 ± 0.04 a.u., and after 225 min at 0.22 ± 0.05 a.u, respectively.

Subsequently, we prepared oligomers of pure and mixed $A\beta_{42}$ and $A\beta_{40}$, ($OA\beta_{42}$, $OA\beta_{3:1}$, $OA\beta_{1:1}$, $OA\beta_{1:3}$, $OA\beta_{40}$) as well as monomers ($MA\beta_{42}$) and fibrils of $A\beta_{42}$ ($FA\beta_{42}$). Characterization of these aggregate types using atomic force microscopy (AFM) uncovered circular structures for Aβ monomers and oligomers and elongated structures for fibrils (Figure 2B). By measuring aggregate height in each AFM topography, serial increases in size were observable from $MA\beta_{42}$, to $OA\beta_{42}$ and $FA\beta_{42}$, sized 0.29 ± 0.08 nm, 0.69 ± 0.22 nm, and 1.43 ± 0.10 nm, respectively (Figure 2C). $OA\beta_{3:1}$, $OA\beta_{1:1}$, $OA\beta_{1:3}$, and $OA\beta_{40}$ were sized 0.87 ± 0.22 nm, 1.04 ± 0.06 nm, 1.14 ± 0.11 nm, and 0.92 ± 0.03 nm, respectively.

Raman spectroscopy revealed changes in Raman peaks associated with α-helical (1,307 cm^{-1}) and β-sheeted (1,240 and 1,671 cm^{-1}) secondary structure, amide backbone (1,555 cm^{-1}), phenylalanine and tyrosine sidechains (1,607–1,615 cm^{-1}), as well as aliphatic side chains with -CH$_2$,-CH$_3$ deformation at 1,447 cm^{-1}, -CH$_2$ asymmetric stretching at 2,850 cm^{-1}, -CH$_2$ symmetric stretching at 2,885 cm^{-1}, and symmetric -CH$_3$ stretching at 2,935 cm^{-1} (Figure 2D) (Fonseca

FIGURE 2

Characterization of the Aβ aggregation process and aggregates of different Aβ42:Aβ40 ratios. **(A)** ThT aggregation profiles for varying ratios of Aβ42:Aβ40 at 20 μM (n = 3). **(B)** Exemplary AFM topographies for monomers, oligomers, and fibrils of Aβ. Topographies were acquired from dried AFM slides covered with 20 μM (monomers, oligomers) or 5 μM (fibrils) peptide solutions. **(C)** Size measurement MAβ42, OAβ42, OAβ3:1, OAβ1:1, OAβ1:3, OAβ40, and FAβ42 using AFM (n = 3). **(D)** Raman spectra of MAβ42, OAβ42, OAβ3:1, OAβ1:1, OAβ1:3, OAβ40, FAβ42, and bovine serum albumin, which contains mainly α-helical secondary structure. Raman peaks differing between the aggregate types are indicated by gray bands (n = 3). Raman spectra were acquired from dried 100 μM peptide films (drop-coating deposition Raman spectroscopy). **(E)** Cross-correlation analysis of Raman spectra derived from MAβ42, OAβ42, and FAβ42 (n = 3). Note the diagonal axis of symmetry indicating self-correlated peaks. Vertical and horizontal lines reveal correlation of one peak with all other peaks. Positive correlation is observable if both examined peaks have the same color in the plot, whereas inverse correlated peaks possess opposite colors. **(F)** Synchronous correlation spectrum at 1670 cm⁻¹, a β-sheet peak. Maxima are positively correlated, whilst minima are inversely correlated with β-sheet peak intensity. Notable maxima and minima are indicated. **(G)** Peak ratio analysis of all examined Aβ aggregates (n = 3) showing the fold change of the respective ratio normalized to MAβ. Statistical significance is indicated compared to MAβ. *p < 0.05, **p < 0.01, ***p < 0.001, am II, amide II; phe, phenylalanine; tyr, tyrosine.
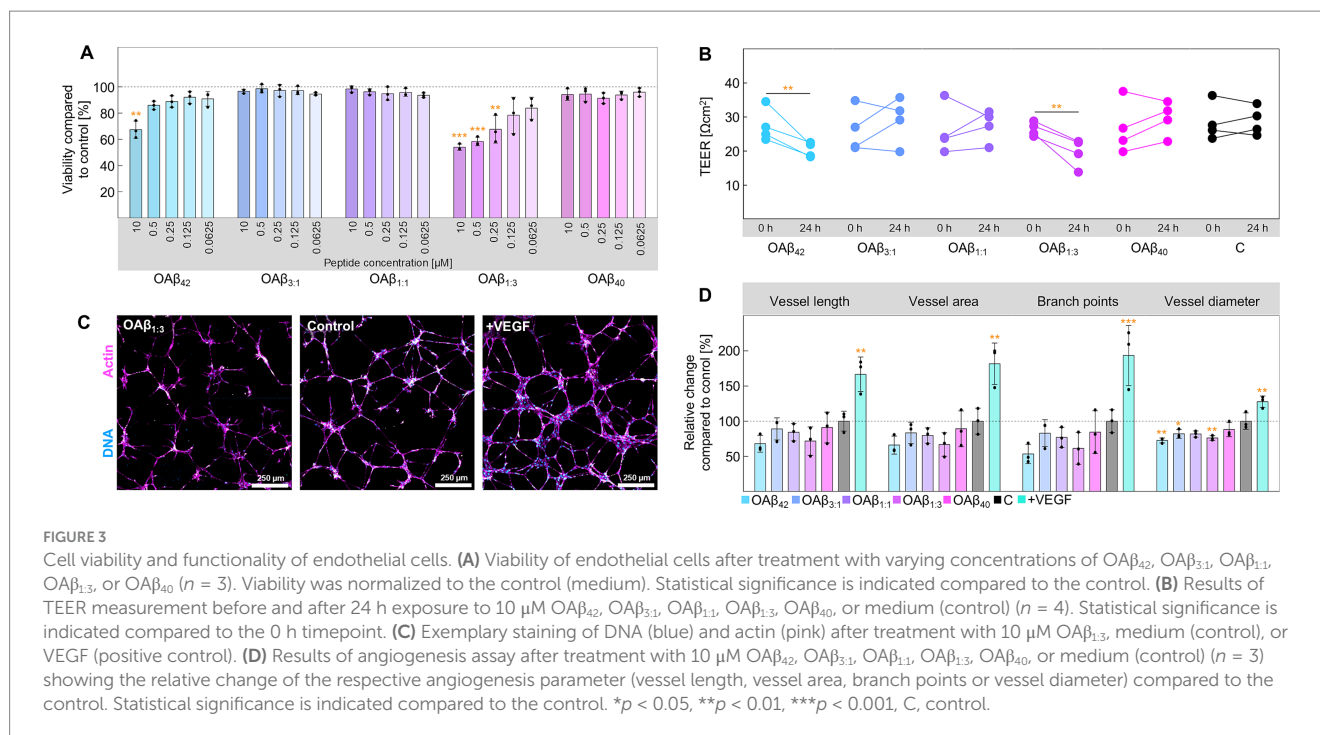
et al., 2019; Rygula et al., 2013; Mensch et al., 2017; Movasaghi et al., 2007; Kuhar et al., 2021; Jamieson et al., 2018). Next, we employed cross-correlation analysis of Raman spectra of Aβ42 monomers, oligomers, and fibrils. The synchronous spectrum depicted in Figure 2E represents a heatmap of the cross-correlation of all Raman shifts; the symmetry line stems from self-correlation. Thus, the correlation of one specific peak with all other peaks can be identified by examining the synchronous spectrum horizontally or vertically. Figure 2F shows the correlation spectrum at 1671 cm⁻¹, a β-sheet peak, which is positively correlated with another β-sheet peak and negatively correlated with peaks of α-helices, aliphatic side chains, and amide backbone. Using ratios of inversely correlated peaks or peak ratios with constant denominators (2,935 cm⁻¹), steady trends depending on aggregate type were found for each peak ratio (Figure 2G). However, differentiation of pure and mixed oligomers was impossible with this analysis.

3.2 Effect of pure and mixed Aβ oligomers on cell viability, function, and metabolism

Next, we systematically examined the effect of pure and mixed Aβ oligomers on four cell types – endothelial cells, neurons, astroglia, and microglia – to examine differential effects on cell viability,

functionality, and metabolism. Endothelial cells form the essential base of the blood–brain barrier, constituting a tight cell monolayer. Whilst OAβ3:1, OAβ1:1, and OAβ40 did not affect cell viability, OAβ42 and OAβ1:3 significantly decreased viability in a concentration-dependent manner, to 67.30 ± 6.53% and 53.96 ± 2.36% at 10 μM, respectively (Figure 3A). Examination of barrier integrity via transepithelial electrical resistance (TEER) measurements exposed a significant reduction of this parameter in endothelial monolayers treated with OAβ42 (from 27.45 ± 4.93 Ωcm² to 20.33 ± 2.18 Ωcm²) and OAβ1:3 (from 26.40 ± 2.04 Ωcm² to 19.58 ± 4.18 Ωcm²) (Figure 3B). Consistently, the assessment of angiogenesis, encompassing vessel length, area, diameter, and branch points further manifested the indications of toxic effects predominantly induced by OAβ42 and OAβ1:3 (Figures 3C,D and Supplementary Figure S1).

In the case of differentiated neurons (Supplementary Figure S2), the viability assay depicts concentration-dependent toxicity of OAβ42 and mixed oligomers (Figure 4A). Specifically, OAβ42, OAβ3:1, OAβ1:1, and OAβ1:3 at a concentration of 10 μM reduced cell viability to 69.70 ± 11.53%, 61.70 ± 9.41%, 64.77 ± 10.88%, and 63.03 ± 2.81%, respectively. OAβ40 exposure only led to a reduction of viability to 79.86 ± 8.88%. Further, results of the neurite outgrowth assay exposed an inhibited growth of these protrusions after incubation with mixed oligomers, approximating the effect of OAβ42 (Figures 4B,C and Supplementary Figure S3). We also evaluated the effect of OAβ42 and

FIGURE 3
Cell viability and functionality of endothelial cells. **(A)** Viability of endothelial cells after treatment with varying concentrations of $OA\beta_{42}$, $OA\beta_{3:1}$, $OA\beta_{1:1}$, $OA\beta_{1:3}$, or $OA\beta_{40}$ ($n = 3$). Viability was normalized to the control (medium). Statistical significance is indicated compared to the control. **(B)** Results of TEER measurement before and after 24 h exposure to 10 μM $OA\beta_{42}$, $OA\beta_{3:1}$, $OA\beta_{1:1}$, $OA\beta_{1:3}$, $OA\beta_{40}$, or medium (control) ($n = 4$). Statistical significance is indicated compared to the 0 h timepoint. **(C)** Exemplary staining of DNA (blue) and actin (pink) after treatment with 10 μM $OA\beta_{1:3}$, medium (control), or VEGF (positive control). **(D)** Results of angiogenesis assay after treatment with 10 μM $OA\beta_{42}$, $OA\beta_{3:1}$, $OA\beta_{1:1}$, $OA\beta_{1:3}$, $OA\beta_{40}$, or medium (control) ($n = 3$) showing the relative change of the respective angiogenesis parameter (vessel length, vessel area, branch points or vessel diameter) compared to the control. Statistical significance is indicated compared to the control. $*p < 0.05$, $**p < 0.01$, $***p < 0.001$, C, control.

the mixed oligomer $OA\beta_{1:3}$, containing a small proportion of $A\beta_{42}$, on cytochrome c mRNA levels, revealing a 1.16 ± 0.30-fold and 1.78 ± 0.58-fold increase, respectively (Figure 4D). Further, Raman analysis of neurons treated with $A\beta$ oligomers also revealed a trend toward increasing intensities of cytochrome c at 750, 1,129, and 1,585 cm^{-1} from $OA\beta_{40}$, over mixed oligomers, to $OA\beta_{42}$ (Supplementary Figure S4; Brazhe et al., 2012).
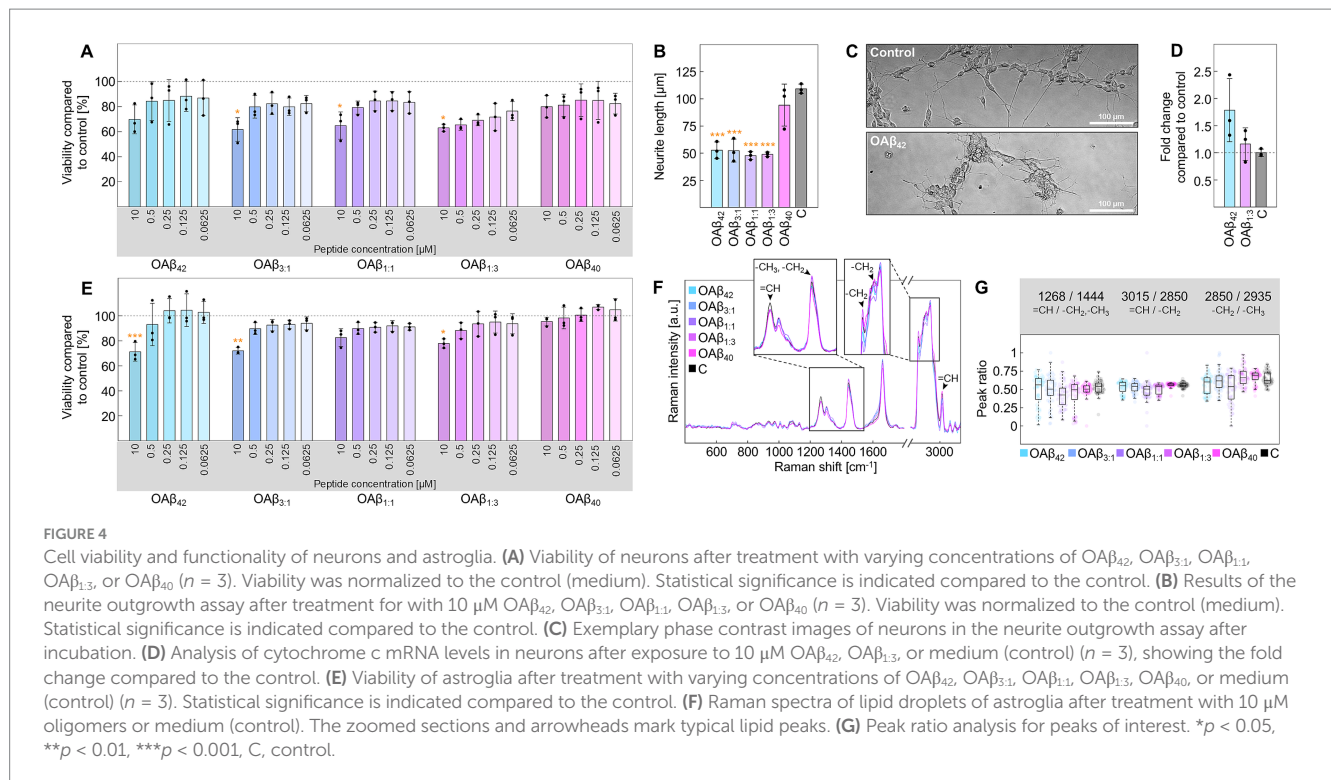
Concerning astroglia, moderate cytotoxicity was registered for $OA\beta_{42}$, $OA\beta_{3:1}$, $OA\beta_{1:1}$, and $OA\beta_{1:3}$ at a concentration of 10 μM ($71.17 \pm 7.44\%$, $71.96 \pm 2.64\%$, $82.47 \pm 7.15\%$, and $77.83 \pm 3.68\%$), with $OA\beta_{1:1}$ leading to the weakest effect, whereas viability was not affected by exposition to $OA\beta_{40}$ (Figure 4E). Further analysis of lipid droplets via confocal Raman microscopy did not reveal differences in lipid droplet distribution (Supplementary Figure S5), however, slight alterations in the corresponding Raman spectra were observed (Figure 4F). Employing peak ratio analysis, we found a lowered ratio of unsaturated to saturated lipids for cells treated with either mixed oligomers or $OA\beta_{42}$, but no trend in alterations in lipid chain length, as shown in Figure 4G.

Similar trends regarding cell viability were also observed in microglia (Figure 5A). While the viability of microglia after exposure to 10 μM $OA\beta_{40}$ or pro-inflammatory stimuli (LPS + IFN-γ) was not significantly reduced ($100.80 \pm 2.38\%$ and $92.12 \pm 1.72\%$), $OA\beta_{42}$, $OA\beta_{3:1}$, and $OA\beta_{1:3}$ showed significant concentration-dependent toxicity ($57.41 \pm 3.29\%$, $52.19 \pm 9.50\%$, and $51.83 \pm 1.42\%$), except for $OA\beta_{1:1}$ ($83.13 \pm 2.93\%$). Concerning TNT formation, $38.54 \pm 9.07\%$ of cells of the control were connected by at least one TNT, $7.41 \pm 2.87\%$ were linked by two TNTs and $8.17 \pm 2.74\%$ were joined by more than three TNTs (Figures 5B,C); similar observations were also made for $OA\beta_{40}$ treated cells. However, $OA\beta_{42}$, $OA\beta_{3:1}$, and $OA\beta_{1:3}$ treatment significantly increased the total number of TNT-connected cells ($64.44 \pm 11.00\%$, $67.56 \pm 6.82\%$, and $62.66 \pm 6.29\%$), as well as the portion of cells connected by three or more TNTs ($22.55 \pm 1.37\%$,

$26.97 \pm 8.25\%$, and $25.18 \pm 7.69\%$). Moreover, Raman imaging revealed an increased ratio of unsaturated/saturated bonds in lipid spectra in microglia treated with mixed oligomers or $OA\beta_{42}$ (Figures 5D–F), contrasting results obtained from the analysis of astroglial lipid droplets (Figures 4E,F). Furthermore, Raman spectra of microglial lipids droplets displayed a slightly lower chain length after treatment with $OA\beta_{42}$, mixed oligomers, and LPS + IFN-γ. An elevated cholesterol peak was only detected after LPS + IFN-γ exposure.

3.3 Impact of $OA\beta_{42}$ and $OA\beta_{1:3}$ and on a model of the BBB

Observations of toxic effects in single cells sparked a further investigation of the impact of $OA\beta_{42}$ and $OA\beta_{1:3}$ on a human-based *in vitro* model of the BBB, composed of endothelial cells in the apical compartment, astroglia lining the basal side of an insert membrane and neurons and microglia in the basolateral compartment (Figure 1). After treatment with $OA\beta_{42}$, $OA\beta_{1:3}$ or LPS + IFN-γ, fluorescence staining and ELISA (Figures 6A,B) uncovered striking differences between LPS + IFN-γ and $A\beta$ oligomer-treated models. Precisely, microglial and neuronal morphology of $OA\beta_{42}$- and $OA\beta_{1:3}$-treated models resembled the control, showing intertwined microglia and neurons, as well as extended neurites. Conversely, neurite length was reduced in models treated with LPS + IFN-γ, with microglia circling neurons. Secretion of pro-inflammatory cytokines IL-6 and IL-8 was also strongly increased in these models, whereas no prominent change was observed for samples treated with $OA\beta_{42}$ and $OA\beta_{1:3}$. TEER was significantly reduced in models treated with $OA\beta_{42}$, $OA\beta_{1:3}$, as well as LPS + IFN-γ from 32.13 ± 4.83 Ωcm^2 to 14.36 ± 2.73 Ωcm^2, 33.83 ± 2.84 Ωcm^2 to 15.84 ± 3.41 Ωcm^2, and 31.47 ± 0.87 Ωcm^2 to 10.11 ± 4.61 Ωcm^2, respectively (Figure 6C), indicating barrier disintegration in each case. While Raman images of microglia

FIGURE 4
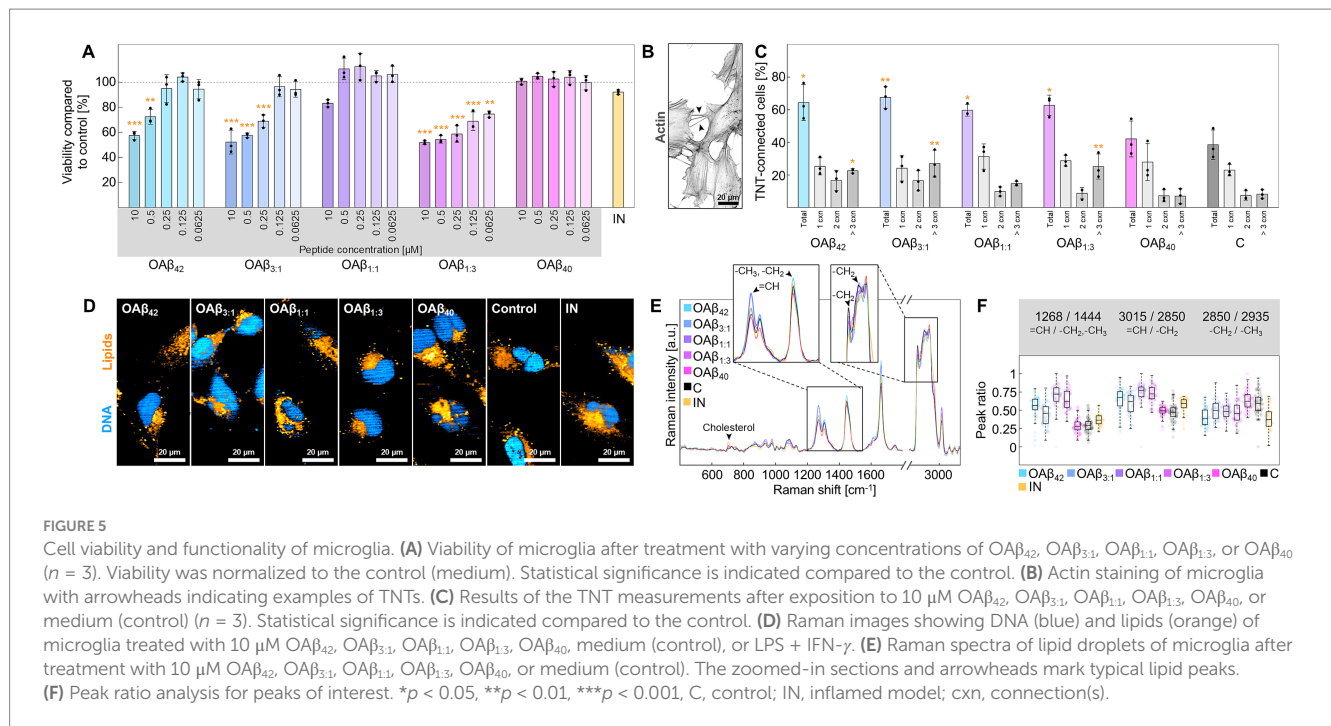Cell viability and functionality of neurons and astroglia. **(A)** Viability of neurons after treatment with varying concentrations of $OA\beta_{42}$, $OA\beta_{3:1}$, $OA\beta_{1:1}$, $OA\beta_{1:3}$, or $OA\beta_{40}$ ($n = 3$). Viability was normalized to the control (medium). Statistical significance is indicated compared to the control. **(B)** Results of the neurite outgrowth assay after treatment for with 10 μM $OA\beta_{42}$, $OA\beta_{3:1}$, $OA\beta_{1:1}$, $OA\beta_{1:3}$, or $OA\beta_{40}$ ($n = 3$). Viability was normalized to the control (medium). Statistical significance is indicated compared to the control. **(C)** Exemplary phase contrast images of neurons in the neurite outgrowth assay after incubation. **(D)** Analysis of cytochrome c mRNA levels in neurons after exposure to 10 μM $OA\beta_{42}$, $OA\beta_{1:3}$, or medium (control) ($n = 3$), showing the fold change compared to the control. **(E)** Viability of astroglia after treatment with varying concentrations of $OA\beta_{42}$, $OA\beta_{3:1}$, $OA\beta_{1:1}$, $OA\beta_{1:3}$, $OA\beta_{40}$, or medium (control) ($n = 3$). Statistical significance is indicated compared to the control. **(F)** Raman spectra of lipid droplets of astroglia after treatment with 10 μM oligomers or medium (control). The zoomed sections and arrowheads mark typical lipid peaks. **(G)** Peak ratio analysis for peaks of interest. *$p < 0.05$, **$p < 0.01$, ***$p < 0.001$, C, control.

resembled the data acquired from microglial monoculture (Figures 5D, 6D), we identified distinct lipid species in neurons (Figure 6E), which were not detectable in monoculture (Supplementary Figure S4). Further differences between treatments with $OA\beta_{1:3}$, $OA\beta_{42}$, and LPS + IFN-γ were revealed using peak ratio analysis. In microglia, $OA\beta_{1:3}$ application led to a shift of lipid spectra toward unsaturated lipids, which was absent for $OA\beta_{42}$. Instead, $OA\beta_{42}$ induced an increase in lipid chain length, which did not occur to the same extent for $OA\beta_{1:3}$. LPS + IFN-γ treated models displayed only a slight shift toward unsaturated lipids with a simultaneous decrease in chain length (Figure 6F). Lipid spectra acquired from neurons displayed fewer differences, and a trend toward unsaturated or saturated lipids was not as clear; however, chain length was again longest after $OA\beta_{42}$ treatment (Figure 6G). Furthermore, investigation of neuronal cytochrome c revealed elevated levels of cytochrome c, as well as a decreased lipid peak intensity, both of which were strongest for treatment with $OA\beta_{1:3}$ (Figure 6H).

4 Discussion

4.1 Role of Aβ40 on Aβ42 fibrillation and structural characterization of mixed oligomers

As protein accumulation is a central characteristic of Aβ-induced pathology, evaluating aggregation kinetics of differing $A\beta_{42}:A\beta_{40}$ ratios is crucial to investigate their toxicity as co-aggregation of $A\beta_{42}$ and $A\beta_{40}$ leads to the formation of oligomers containing both isoforms (Vadukul et al., 2020). Our results clearly indicate a sequential reduction of the aggregation speed of $A\beta_{42}$ after the addition of $A\beta_{40}$, implying an inhibitory effect of the shorter peptide variant on $A\beta_{42}$

fibrillation (Figure 2A) (Chang and Chen, 2014; Braun et al., 2022). Thus, considering the direct impact of aggregate stability, size, and conformation on Aβ toxicity, the observed decrease of plateau height and aggregation speed may contribute to understanding the toxicity of co-aggregated $A\beta_{42}$ and $A\beta_{40}$ (Cizas et al., 2010; Chang and Chen, 2014; Vadukul et al., 2020). While prior studies mostly focused on pure oligomers, the formation of mixed oligomers, and especially the ratio of $A\beta_{42}:A\beta_{40}$, seems to be a crucial factor in neurodegeneration and overall AD-related pathophysiology (Chang and Chen, 2014; Kuperstein et al., 2010; Kwak et al., 2020). The strikingly different aggregation kinetics motivated us to delve further into the structural characterization and composition of Aβ aggregates using AFM and Raman spectroscopy. Our aggregation protocols for monomers, pure and mixed oligomers, as well as fibrils, yielded sizes matching the described range in literature (Figures 2B,C) (Ungureanu et al., 2016; Cizas et al., 2010; Manassero et al., 2016). Despite being a valuable tool for analyzing Aβ aggregates due to its sensitivity to secondary structure, Raman spectroscopy (Figures 2D–G) is rarely used in the context of neurodegenerative diseases. Existing Raman spectroscopic studies have mostly been confined to the examination of fibrillar Aβ (Flynn and Lee, 2018). Notably, Yu et al. (2018) investigated the Aβ aggregation kinetics using surface-enhanced-Raman-spectroscopy (SERS), a technique designed to amplify the Raman signal. However, using SERS affects the location and intensities of Raman peaks, impeding interpretation and making it unsuitable for assessing aggregate conformation. Hence, we sought to explore the potential of Raman spectroscopy in the analysis of amyloid aggregates using drop-coating deposition Raman spectroscopy (DCDRS), entrapping biomolecules in a hydrated environment while decreasing detection limits (Peters et al., 2016; Ortiz et al., 2006). Through cross-correlation analysis, we revealed changes in the secondary structure of beta-amyloid owing to the typical conversion of unordered regions and

FIGURE 5
Cell viability and functionality of microglia. **(A)** Viability of microglia after treatment with varying concentrations of OAβ$_{42}$, OAβ$_{3:1}$, OAβ$_{1:1}$, OAβ$_{1:3}$, or OAβ$_{40}$ (n = 3). Viability was normalized to the control (medium). Statistical significance is indicated compared to the control. **(B)** Actin staining of microglia with arrowheads indicating examples of TNTs. **(C)** Results of the TNT measurements after exposition to 10 μM OAβ$_{42}$, OAβ$_{3:1}$, OAβ$_{1:1}$, OAβ$_{1:3}$, OAβ$_{40}$, or medium (control) (n = 3). Statistical significance is indicated compared to the control. **(D)** Raman images showing DNA (blue) and lipids (orange) of microglia treated with 10 μM OAβ$_{42}$, OAβ$_{3:1}$, OAβ$_{1:1}$, OAβ$_{1:3}$, OAβ$_{40}$, medium (control), or LPS + IFN-γ. **(E)** Raman spectra of lipid droplets of microglia after treatment with 10 μM OAβ$_{42}$, OAβ$_{3:1}$, OAβ$_{1:1}$, OAβ$_{1:3}$, OAβ$_{40}$, or medium (control). The zoomed-in sections and arrowheads mark typical lipid peaks. **(F)** Peak ratio analysis for peaks of interest. *p < 0.05, **p < 0.01, ***p < 0.001, C, control; IN, inflamed model; cxn, connection(s).

α-helices to β-sheets (Mallesh et al., 2023). Interestingly, the analysis also uncovered previously unidentified shifts in the Raman spectra. For instance, the amide II band, typically faint due to low scattering effects, was distinguishable for monomeric Aβ$_{42}$ and faded during Aβ aggregation, indicating an increased rigidity in the amide backbone (Mensch et al., 2017). The decrease in relative intensity of amino acid side chains, such as phenol rings or acyl chains, further suggested constriction of molecular vibrations during this process. We pinpointed these sequential changes in amyloid structure using peak ratio analysis, demonstrating reproducible trends from monomers to fibrils. Overall, Raman spectroscopy offers a straightforward approach to differentiating aggregate types since DCDRS requires minimal sample preparation as opposed to AFM. However, distinguishing aggregate types depending on Aβ$_{42}$:Aβ$_{40}$ ratio proved challenging, and further research is needed to address this question.

4.2 Effect of Aβ$_{42}$ fraction in mixed oligomers on the endothelium

To examine the effects of Aβ oligomers depending on the Aβ$_{42}$:Aβ$_{40}$ ratio, we treated AD-relevant brain cells with pure and mixed oligomers. Importantly, the peptide concentrations used in this study were much higher than physiological levels of soluble Aβ found in brain tissue of AD patients (Roberts et al., 2017). However, such high concentrations are considered necessary to stimulate immortalized cell lines (McCarthy et al., 2016). As main constituents of the BBB, we initially analyzed the cytotoxic effects of pure and mixed oligomers on endothelial cells: only OAβ$_{42}$ and OAβ$_{1:3}$ significantly decreased viability and displayed dose-dependent toxicity (Figure 3A). These findings were confirmed by our investigation of barrier integrity, which showed significant decreases of TEER only

after exposure to OAβ$_{42}$ and OAβ$_{1:3}$. This effect has been described for OAβ$_{42}$, but not for OAβ$_{1:3}$ (Figure 3B) (Parodi-Rullán et al., 2020). Further, reduction of angiogenesis has also been depicted in prior reports and was found in our study after exposure to OAβ$_{42}$, as reported, and OAβ$_{1:3}$ (Figures 3C,D) (Parodi-Rullán et al., 2020; Paris et al., 2004). The fact that vascular amyloid deposits mainly constitute Aβ$_{40}$, combined with the detrimental effects observed in OAβ$_{1:3}$ treated endothelial cells, calls for further studies investigating the role of these oligomers for BBB breakdown (Qi and Ma, 2017).

4.3 Mitochondrial dysfunction in neuronal cells induced by Aβ oligomers

In case of neuronal cells, our results show a decrease in viability and neurite outgrowth upon exposure to OAβ$_{42}$, consistent with previous reports (Figures 4A–C) (Zhang et al., 2022; Petratos et al., 2008; Krishtal et al., 2017). Equally detrimental effects were observed for each mixed oligomer, aligning with studies by Kuperstein et al. (2010) and Kwak et al. (2020), the latter showing that the Aβ$_{42}$:Aβ$_{40}$ ratio drives tau pathology in neurons. Thus, our results underscore the importance of the Aβ$_{42}$:Aβ$_{40}$ ratio for AD-associated pathophysiology. Analysis of cytochrome c mRNA levels indicated enhanced expression of cytochrome c after treatment with OAβ$_{42}$ and OAβ$_{1:3}$, amplifying cell death (Chandra et al., 2002). Additionally, Raman imaging of neurons (Supplementary Figure S4) showed that all oligomers, except OAβ$_{40}$, increased cytochrome c-related Raman peaks, further indicating cytochrome c accumulation. Therefore, our results implicate mitochondrial dysfunction induced by both OAβ$_{42}$ and oligomers containing only minor amounts of Aβ$_{42}$, such as OAβ$_{1:3}$. These effects may stem from N-methyl-D-aspartate (NMDA) receptor overactivity caused by activation by Aβ oligomers (Gao et al., 2007; Li et al., 2011).
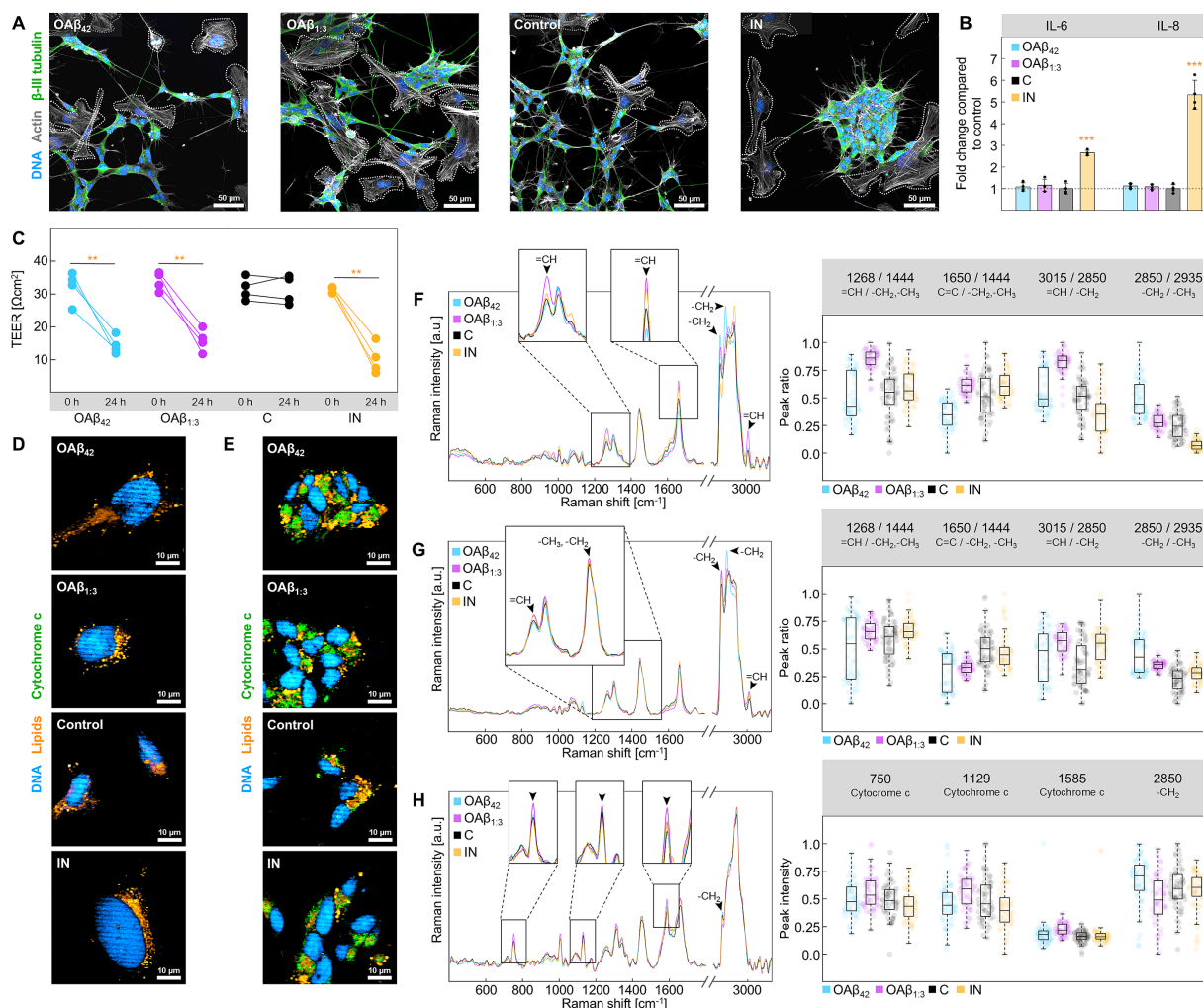
FIGURE 6

Analysis of the BBB model. **(A)** Staining of DNA (blue), actin (gray) and β-III tubulin (green) in the basal compartment of the BBB model after treatment with 10 μM OAβ$_{42}$, 10 μM OAβ$_{1:3}$, medium + PBS (control), or LPS + IFN-γ. Microglia are circled with dashed lines. **(B)** Results of ELISA for IL-6 and IL-8 after treatment with 10 μM OAβ$_{42}$, 10 μM OAβ$_{1:3}$, medium + PBS (control), or LPS + IFN-γ ($n = 3$) showing the fold change compared to the control. **(C)** Results of TEER measurement for exposure to 10 μM OAβ$_{42}$, 10 μM OAβ$_{1:3}$, medium + PBS (control), or LPS + IFN-γ ($n = 4$). Statistical significance is indicated compared to the 0 h timepoint. Raman images of **(D)** microglia and **(E)** neurons in the basal compartment of the BBB model showing DNA (blue), lipids (orange), and cytochrome c (green) after exposure to 10 μM OAβ$_{42}$, 10 μM OAβ$_{1:3}$, medium + PBS (control), or LPS + IFN-γ. Raman spectra of lipid droplets of microglia **(F)**, lipid droplets of neurons **(G)** and cytochrome c of neurons **(H)** are displayed on the left, with zoomed-in sections showing peaks of interest. Corresponding peak ratio or intensity analysis is shown on the right side. *$p < 0.05$, **$p < 0.01$, ***$p < 0.001$, C, control; IN, inflamed model.

4.4 Cellular and metabolic changes of glial cells following Aβ oligomer exposure

Due to their essential contribution to neurodegeneration and based on the previously reported severe effect of OAβ$_{42}$, we investigated the effects of differently mixed Aβ oligomers on astroglia (Abramov et al., 2004; Hou et al., 2011). We were able to show prominent effects of such mixed oligomers on these cells, mirroring the results of the viability assay on neurons (Figure 4D). Raman analysis indicated a shift in the composition of astroglial lipid droplets toward saturated lipids instigated by all oligomers except OAβ$_{40}$ (Figures 4E,F). This inclination is especially interesting, considering astroglia-promoted neurodegeneration via secretion of saturated fatty acids (Guttenplan et al., 2021). Hence, our findings reinforce the hypothesis that Aβ oligomers

only containing minor amounts of Aβ$_{42}$ may be equally toxic as pure Aβ$_{42}$ oligomers. Besides astroglia, microglia are also strongly linked to AD due to their substantial contribution to neuroinflammation (de Dios et al., 2023). Additionally, especially activated APOE (apolipoprotein E) positive microglia play an important role in Aβ plaque formation and compaction (Kaji et al., 2024; Spangenberg et al., 2019). Our investigation not only confirmed the already reported toxicity of OAβ$_{42}$ but also uncovered the severe cytotoxic effects of OAβ$_{3:1}$ and OAβ$_{1:3}$ (Figure 5A) (Pan et al., 2011). The observed proliferative effect (viability above >100% compared to control) after OAβ$_{40}$ treatment may be linked to a physiological response of the microglia to clear Aβ, albeit this effect was not significant (Fruhwürth et al., 2024). Interestingly, Aβ oligomers also induce the formation of TNTs, serving as a transportation system for Aβ in the central nervous

system (Zhang et al., 2021). Previous studies have reported increased TNT-based connections between microglial cells when exposed to Aβ or other toxic peptides like α-synuclein (Chakraborty et al., 2023; Dilna et al., 2021). Our study showed not only an increase in microglia connected with one TNT across the treatment with all oligomers – except OAβ$_{40}$ – but also a substantial number of cells linked by multiple TNTs (Figures 5B,C). In fact, a previous study found that Aβ$_{42}$ oligomers are incorporated into endo-lysosomal vesicles, which subsequently transport Aβ between neurons via TNTs (Dilna et al., 2021). Furthermore, other pathological proteins such as prions are also transported inside endo-lysosomal vesicles through TNTs between cells (Zhu et al., 2015). Therefore, it is likely that the TNTs observed in this study served a similar purpose. In addition to TNT formation, microglial lipid metabolism is associated with AD, and we detected an increase in unsaturated lipids in microglial lipid droplets, contrasting the results obtained with astroglia (Figures 5D–F). Interestingly, the lipid profile of LPS + IFN-γ-stimulated microglia markedly differed from cells exposed to oligomeric Aβ, implying different inflammatory cellular responses. These observations are also supported by the viability assay, which showed no significant decrease upon LPS + IFN-γ treatment. Conversely, Aβ oligomers induced a different pathological state, which is highlighted by Raman analysis of lipid droplets. Relative lipid chain length was decreased for cells treated with mixed oligomers, OAβ$_{42}$, as well as LPS + IFN-γ, however, a strong rise in unsaturated lipids was only observed for mixed oligomers and OAβ$_{42}$. These alterations in lipid droplet composition toward unsaturated lipids have been identified as a hallmark of inflammation, suggesting production of pro-inflammatory lipids such as arachnoid acid and prostaglandins (Czamara et al., 2017; Chausse et al., 2021). Moreover, the increase of unsaturation is possibly also linked to APOE, which induces abnormal accumulation of unsaturated fatty acids in lipid droplets in AD (Sienski et al., 2021). APOE also facilitates the uptake and compaction of Aβ in the microglial endo-lysosomal system, which leads to the formation of indigestible Aβ aggregates which are released to the surrounding and contribute to plaque growth (Kaji et al., 2024). Thus, APOE not only influences abnormal lipid metabolism but also drives amyloidosis, and future studies should further address the link between the two effects. Meanwhile, LPS + IFN-γ-stimulated cells displayed only a moderate rise in unsaturation and an increase of cholesterol, which was not detected in mixed oligomers and OAβ$_{42}$-treated cells. Although underlining the differences in the induced inflammatory state, this finding is unexpected as raised levels of cholesterol in microglia are considered a feature of neurodegenerative diseases (Zareba and Peri, 2021; Muñoz Herrera and Zivkovic, 2022). Presumably, the relative increase in cholesterol in Aβ oligomer-treated cells was below the detection limit, while exposure to a strong pro-inflammatory stimulus like LPS + IFN-γ caused a higher relative cholesterol increase. Importantly, the results presented here only encompass the treatment of cultured cells with soluble Aβ oligomers, but not an analysis of intracellular formation or trafficking of these oligomers. Presumably, amyloid precursor protein (APP) is consecutively cleaved by β-secretase and γ-secretase at the lysosomal membrane, leading to the accumulation of Aβ inside lysosomes and subsequent secretion

into the extracellular compartment (Tan and Gleeson, 2019). Furthermore, the lysosomal acidic pH promotes aggregation of Aβ and formation of Aβ oligomers already before secretion, causing severe intracellular damage (Schützmann et al., 2021). The role of APOE and lipoprotein flux is particularly interesting in this context, as endocytosis of lipoproteins into lysosomes has been shown to serve as seeding platform for Aβ and to promote plaque growth (Kaji et al., 2024). Therefore, future research investigating Aβ$_{42}$:Aβ$_{40}$-ratio-dependent intracellular formation of oligomers, their trafficking and effects may complement the findings presented in this study.

4.5 Differential effects of mixed Aβ oligomers on BBB integrity and microglia activation

Overall, these monoculture-based studies on endothelial cells, neurons, astroglia, and microglia illustrate the individual effects of mixed Aβ oligomers in the different brain cell types. In each experiment, OAβ$_{1:3}$ exposition was equally detrimental to cell viability and function as OAβ$_{42}$ oligomers, and – in the case of endothelial cells – OAβ$_{1:3}$ was the only mixed oligomer type showing similar toxicity as OAβ$_{42}$. Due to their inherent structural differences, these two oligomer types possibly possess different effects on cells and were, therefore, selected as candidates for a comprehensive evaluation. By extending our study to an *in vitro* model of the BBB, encompassing all investigated cell types, we further explored differences between OAβ$_{42}$ and OAβ$_{1:3}$ toxicity. We observed a significant drop in TEER after 24 h of exposure to OAβ$_{42}$, OAβ$_{1:3}$, and LPS + IFN-γ, pointing to barrier dysfunction in each case (Figure 6C). Additionally, the absolute decrease of TEER induced by OAβ$_{42}$ and OAβ$_{1:3}$ was more severe than in endothelial cell monocultures. Our observations also align with reported damaging effects of inflammatory stimuli on brain endothelial barrier integrity (Hu et al., 2019). These detrimental effects may lead to both direct damage and the induction of inflammatory responses, which have been reported to shift the phenotype of resting microglia into an activated state (Caldeira et al., 2017). Specifically, literature suggests an amoeboid microglial morphology upon activation, while resting microglia are rather ramified (Wendimu and Hooks, 2022). However, the activation of microglial cells is a highly complex process dependent on various parameters (Gao et al., 2023). In our study, analysis of microglial morphology in the BBB model's basal compartment revealed differences between oligomer treatment and LPS + IFN-γ stimulation, further suggesting distinctly different immunomodulatory mechanisms (Figure 6A). Accordingly, IL-6 and IL-8 secretion was strongly increased for LPS + IFN-γ treated models but rose only slightly after oligomer exposition (Figure 6B). While these results support both the concept of complex microglial phenotypes and the hypothesis of a dysfunctional microglial phenotype upon stimulation with Aβ, they contrast with evidence specifying an increase of pro-inflammatory interleukin secretion (Franciosi et al., 2005; Kiraly et al., 2023). To gain further insight into changes in cell metabolism, we performed Raman imaging on neurons and microglia (Figures 6D–H). Regarding microglia, the notable rise

in the relative amount of unsaturated lipids within lipid droplets triggered by $OA\beta_{1:3}$ may be linked to involvement in eicosanoid metabolism (Farmer et al., 2020; Khatchadourian et al., 2012). This circumstance is especially interesting, considering free arachidonic acid levels and prostaglandin E2 levels are elevated in AD (Yin, 2023). Conversely, $OA\beta_{42}$ treatment primarily induced an increase of chain length, implying a higher abundance of long-chained lipids in lipid droplets. Notably, apart from polyunsaturated lipids such as prostaglandins, such long-chained saturated lipids are also involved in pro-inflammatory processes mediated by glial cells (Gupta et al., 2012). Moreover, LPS + IFN-γ did not strongly alter the ratio of unsaturated to saturated lipids but decreased relative chain length, further suggesting a different pro-inflammatory mechanism as opposed to oligomeric Aβ. Our findings also reveal the presence of lipids in neurons, which was not observed in monoculture, thereby supporting evidence of lipid transfer between cells in co-culture (Ralhan et al., 2021). Qualitative differences were not as pronounced as in microglia, yet again, $OA\beta_{42}$ led to accumulation of lipids with higher relative chain length, whereas $OA\beta_{1:3}$ induced enrichment of unsaturated lipids. Interestingly, both phenomena may be evoked by a stress reaction of neurons. Since polyunsaturated lipids are especially vulnerable to peroxidation caused by reactive oxygen species, neurons sequester them into lipid droplets (Bailey et al., 2015). Contrarily, saturated long-chain fatty acids are reportedly highly toxic, alleviated by deposition in lipid droplets, underscoring the complex function of lipid droplets in neurons (Ackerman et al., 2018). Our findings using Raman microscopy also include slight increases in reduced cytochrome c intensities and a reduction of the lipid peak intensity in neurons, particularly associated with $OA\beta_{1:3}$. These results indicate defects in the respiratory chain and lipid peroxidation, respectively, the latter of which suit the notion of unsaturated lipid rescue into lipid droplets (Abramczyk et al., 2022; Russo et al., 2019).

A possible explanation for the differential biochemical composition of BBB-associated microglia after $OA\beta_{42}$ and $OA\beta_{1:3}$ treatment as well as the pronounced toxicity of $OA\beta_{42}$ and $OA\beta_{1:3}$ on endothelial cells and microglia monocultures may be found in the results of the ThT aggregation assay: it demonstrated that $A\beta_{42}$ is more prone to *in situ* fibrillation, while $A\beta_{1:3}$ forms smaller stable aggregates. Thus, this points toward a dual toxicity of the different oligomeric ratios of $A\beta_{42}$:$A\beta_{40}$ – *in situ* fibrillation of mainly $OA\beta_{42}$, and stabilization of low-$A\beta_{42}$-high-$A\beta_{40}$ oligomers, like $OA\beta_{1:3}$, by their $A\beta_{40}$ content (Chang and Chen, 2014; Krishtal et al., 2017). Taken together, stable $OA\beta_{1:3}$ is not only similarly toxic as $OA\beta_{42}$, but these oligomers also seem to cause toxicity via a different mechanism than $OA\beta_{42}$. Furthermore, we observed a less pronounced toxicity of $OA\beta_{42}$ and $OA\beta_{1:3}$ in neurons and astroglia, which in turn suggests that endothelial cells and microglia are especially prone to $A\beta_{42}$:$A\beta_{40}$-ratio-dependent toxicity. Therefore, this study proves that the $A\beta_{42}$:$A\beta_{40}$ ratio in oligomers strongly influences cell metabolism and functionality, which is especially crucial considering that Aβ oligomers only containing minor amounts of $A\beta_{42}$ are formed at the very beginning of AD. Hence, the overall evidence presented in our study clearly questions the $A\beta_{42}$ oligomer-focused research in the field of AD and reveals a toxicity of Aβ oligomers, which has been previously overlooked.

Data availability statement

The raw data supporting the conclusions of this article will be made available by the authors, without undue reservation.

Ethics statement

Ethical approval was not required for the studies on humans in accordance with the local legislation and institutional requirements because only commercially available established cell lines were used.

Author contributions

Funding

Acknowledgments

Conflict of interest

The authors declare that the research was conducted in the absence of any commercial or financial relationships that could be construed as a potential conflict of interest.

Generative AI statement

The author(s) declare that no Gen AI was used in the creation of this manuscript.

Publisher's note

All claims expressed in this article are solely those of the authors and do not necessarily represent those of their affiliated organizations, or those of the publisher, the editors and the reviewers. Any product that may be evaluated in this article, or claim that may be made by its manufacturer, is not guaranteed or endorsed by the publisher.

Supplementary material

The Supplementary material for this article can be found online at: https://www.frontiersin.org/articles/10.3389/fncel.2024.1516093/full#supplementary-material

References

Abramczyk, H., Sobkiewicz, B., Walczak-Jędrzejowska, R., Marchlewska, K., and Surmacki, J. (2022). Decoding the role of cytochrome c in metabolism of human spermatozoa by Raman imaging. *Front. Cell Dev. Biol.* 10:983993. doi: 10.3389/fcell.2022.983993

Abramov, A. Y., Canevari, L., and Duchen, M. R. (2004). Beta-amyloid peptides induce mitochondrial dysfunction and oxidative stress in astrocytes and death of neurons through activation of NADPH oxidase. *J. Neurosci.* 24, 565–575. doi: 10.1523/JNEUROSCI.4042-03.2004

Ackerman, D., Tumanov, S., Qiu, B., Michalopoulou, E., Spata, M., Azzam, A., et al. (2018). Triglycerides promote lipid homeostasis during hypoxic stress by balancing fatty acid saturation. *Cell Rep.* 24, 2596–2605.e5. doi: 10.1016/j.celrep.2018.08.015

Alasmari, F., Alshammari, M. A., Alasmari, A. F., Alanazi, W. A., and Alhazzani, K. (2018). Neuroinflammatory cytokines induce amyloid Beta neurotoxicity through modulating amyloid precursor protein levels/metabolism. *Biomed. Res. Int.* 2018, 3087475–3087478. doi: 10.1155/2018/3087475

Bailey, A. P., Koster, G., Guillermier, C., Hirst, E. M. A., MacRae, J. I., Lechene, C. P., et al. (2015). Antioxidant role for lipid droplets in a stem cell niche of Drosophila. *Cell* 163, 340–353. doi: 10.1016/j.cell.2015.09.020

Beretta, C., Svensson, E., Dakhel, A., Zyśk, M., Hanrieder, J., Sehlin, D., et al. (2024). Amyloid-β deposits in human astrocytes contain truncated and highly resistant proteoforms. *Mol. Cell. Neurosci.* 128:103916. doi: 10.1016/j.mcn.2024.103916

Bouter, Y., Dietrich, K., Wittnam, J. L., Rezaei-Ghaleh, N., Pillot, T., Papot-Couturier, S., et al. (2013). N-truncated amyloid β (Aβ) 4-42 forms stable aggregates and induces acute and long-lasting behavioral deficits. *Acta Neuropathol.* 126, 189–205. doi: 10.1007/s00401-013-1129-2

Braun, G. A., Dear, A. J., Sanagavarapu, K., Zetterberg, H., and Linse, S. (2022). Amyloid-β peptide 37, 38 and 40 individually and cooperatively inhibit amyloid-β 42 aggregation. *Chem. Sci.* 13, 2423–2439. doi: 10.1039/D1SC02990H

Brazhe, N. A., Treiman, M., Brazhe, A. R., Find, N. L., Maksimov, G. V., and Sosnovtseva, O. V. (2012). Mapping of redox state of mitochondrial cytochromes in live cardiomyocytes using Raman microspectroscopy. *PLoS One* 7:e41990. doi: 10.1371/journal.pone.0041990

Caldeira, C., Cunha, C., Vaz, A. R., Falcão, A. S., Barateiro, A., Seixas, E., et al. (2017). Key aging-associated alterations in primary microglia response to Beta-amyloid stimulation. *Front. Aging Neurosci.* 9:277. doi: 10.3389/fnagi.2017.00277

Chakraborty, R., Nonaka, T., Hasegawa, M., and Zurzolo, C. (2023). Tunnelling nanotubes between neuronal and microglial cells allow bi-directional transfer of α-Synuclein and mitochondria. *Cell Death Dis.* 14:329. doi: 10.1038/s41419-023-05835-8

Chandra, D., Liu, J.-W., and Tang, D. G. (2002). Early mitochondrial activation and cytochrome c up-regulation during apoptosis. *J. Biol. Chem.* 277, 50842–50854. doi: 10.1074/jbc.M207622200

Chang, Y.-J., and Chen, Y.-R. (2014). The coexistence of an equal amount of Alzheimer's amyloid-β 40 and 42 forms structurally stable and toxic oligomers through a distinct pathway. *FEBS J.* 281, 2674–2687. doi: 10.1111/febs.12813

Chausse, B., Kakimoto, P. A., and Kann, O. (2021). Microglia and lipids: how metabolism controls brain innate immunity. *Semin. Cell Dev. Biol.* 112, 137–144. doi: 10.1016/j.semcdb.2020.08.001

Cizas, P., Budvytyte, R., Morkuniene, R., Moldovan, R., Broccio, M., Lösche, M., et al. (2010). Size-dependent neurotoxicity of beta-amyloid oligomers. *Arch. Biochem. Biophys.* 496, 84–92. doi: 10.1016/j.abb.2010.02.001

Corliss, B. A., Doty, R. W., Mathews, C., Yates, P. A., Zhang, T., and Peirce, S. M. (2020). REAVER: a program for improved analysis of high-resolution vascular network images. *Microcirculation* 27:e12618. doi: 10.1111/micc.12618

Czamara, K., Majzner, K., Selmi, A., Baranska, M., Ozaki, Y., and Kaczor, A. (2017). Unsaturated lipid bodies as a hallmark of inflammation studied by Raman 2D and 3D microscopy. *Sci. Rep.* 7:40889. doi: 10.1038/srep40889

de Dios, C., Abadin, X., Roca-Agujetas, V., Jimenez-Martinez, M., Morales, A., Trullas, R., et al. (2023). Inflammasome activation under high cholesterol load triggers a protective microglial phenotype while promoting neuronal pyroptosis. *Transl. Neurodegener.* 12:10. doi: 10.1186/s40035-023-00343-3

Deleanu, M., Deschaume, O., Cipelletti, L., Hernandez, J.-F., Bartic, C., Cottet, H., et al. (2022). Taylor dispersion analysis and atomic force microscopy provide a quantitative insight into the aggregation kinetics of Aβ (1-40)/Aβ (1-42) amyloid peptide mixtures. *ACS Chem. Neurosci.* 13, 786–795. doi: 10.1021/acschemneuro.1c00784

DeTure, M. A., and Dickson, D. W. (2019). The neuropathological diagnosis of Alzheimer's disease. *Mol. Neurodegener.* 14:32. doi: 10.1186/s13024-019-0333-5

Dilna, A., Deepak, K. V., Damodaran, N., Kielkopf, C. S., Kagedal, K., Ollinger, K., et al. (2021). Amyloid-β induced membrane damage instigates tunneling nanotube-like conduits by p21-activated kinase dependent actin remodulation. *Biochim. Biophys. Acta Mol. basis Dis.* 1867:166246. doi: 10.1016/j.bbadis.2021.166246

Dravid, A., Raos, B., Svirskis, D., and O'Carroll, S. J. (2021). Optimised techniques for high-throughput screening of differentiated SH-SY5Y cells and application for neurite outgrowth assays. *Sci. Rep.* 11:23935. doi: 10.1038/s41598-021-03442-1

Encinas, M., Iglesias, M., Liu, Y., Wang, H., Muhaisen, A., Ceña, V., et al. (2000). Sequential treatment of SH-SY5Y cells with retinoic acid and brain-derived neurotrophic factor gives rise to fully differentiated, neurotrophic factor-dependent, human neuron-like cells. *J. Neurochem.* 75, 991–1003. doi: 10.1046/j.1471-4159.2000.0750991.x

Farmer, B. C., Walsh, A. E., Kluemper, J. C., and Johnson, L. A. (2020). Lipid Droplets in Neurodegenerative Disorders. *Front. Neurosci.* 14:742. doi: 10.3389/fnins.2020.00742

Faulkner, A., Purcell, R., Hibbert, A., Latham, S., Thomson, S., Hall, W. L., et al. (2014). A thin layer angiogenesis assay: a modified basement matrix assay for assessment of endothelial cell differentiation. *BMC Cell Biol.* 15:41. doi: 10.1186/s12860-014-0041-5

Flynn, J. D., and Lee, J. C. (2018). Raman fingerprints of amyloid structures. *Chem. Commun.* 54, 6983–6986. doi: 10.1039/c8cc03217c

Fonseca, E. A., Lafetá, L., Cunha, R., Miranda, H., Campos, J., Medeiros, H. G., et al. (2019). A fingerprint of amyloid plaques in a bitransgenic animal model of Alzheimer's disease obtained by statistical unmixing analysis of hyperspectral Raman data. *Analyst* 144, 7049–7056. doi: 10.1039/C9AN01631G

Franciosi, S., Choi, H. B., Kim, S. U., and McLarnon, J. G. (2005). IL-8 enhancement of amyloid-beta (Abeta 1-42)-induced expression and production of pro-inflammatory cytokines and COX-2 in cultured human microglia. *J. Neuroimmunol.* 159, 66–74. doi: 10.1016/j.jneuroim.2004.10.006

Fruhwürth, S., Zetterberg, H., and Paludan, S. R. (2024). Microglia and amyloid plaque formation in Alzheimer's disease - evidence, possible mechanisms, and future challenges. *J. Neuroimmunol.* 390:578342. doi: 10.1016/j.jneuroim.2024.578342

Gao, C., Jiang, J., Tan, Y., and Chen, S. (2023). Microglia in neurodegenerative diseases: mechanism and potential therapeutic targets. *Sig. Transduct. Target. Ther.* 8:359. doi: 10.1038/s41392-023-01588-0

Gao, X., Xu, X., Pang, J., Zhang, C., Ding, J. M., Peng, X., et al. (2007). NMDA receptor activation induces mitochondrial dysfunction, oxidative stress and apoptosis in cultured neonatal rat cardiomyocytes. *Physiol. Res.* 56, 559–569. doi: 10.33549/physiolres.931053

Gupta, S., Knight, A. G., Gupta, S., Keller, J. N., and Bruce-Keller, A. J. (2012). Saturated long-chain fatty acids activate inflammatory signaling in astrocytes. *J. Neurochem.* 120, 1060–1071. doi: 10.1111/j.1471-4159.2012.07660.x

Guttenplan, K. A., Weigel, M. K., Prakash, P., Wijewardhane, P. R., Hasel, P., Rufen-Blanchette, U., et al. (2021). Neurotoxic reactive astrocytes induce cell death via saturated lipids. *Nature* 599, 102–107. doi: 10.1038/s41586-021-03960-y

Hampel, H., Hardy, J., Blennow, K., Chen, C., Perry, G., Kim, S. H., et al. (2021). The amyloid-β pathway in Alzheimer's disease. *Mol. Psychiatry* 26, 5481–5503. doi: 10.1038/s41380-021-01249-0

Hernandez-Zimbron, L. F., Luna-Muñoz, J., Mena, R., Vazquez-Ramirez, R., Kubli-Garfias, C., Cribbs, D. H., et al. (2012). Amyloid-β peptide binds to cytochrome C oxidase subunit 1. *PLoS One* 7:e42344. doi: 10.1371/journal.pone.0042344

Hou, L., Liu, Y., Wang, X., Ma, H., He, J., Zhang, Y., et al. (2011). The effects of amyloid-β42 oligomer on the proliferation and activation of astrocytes in vitro. *In Vitro Cell. Dev. Biol. Animal* 47, 573–580. doi: 10.1007/s11626-011-9439-y

Hu, Y., Bi, Y., Yao, D., Wang, P., and Li, Y. (2019). Omi/HtrA2 protease associated cell apoptosis participates in blood-brain barrier dysfunction. *Front. Mol. Neurosci.* 12:48. doi: 10.3389/fnmol.2019.00048

Huang, Y., and Liu, R. (2020). The toxicity and polymorphism of β-amyloid oligomers. *Int. J. Mol. Sci.* 21:4477. doi: 10.3390/ijms21124477

Jamieson, L. E., Li, A., Faulds, K., and Graham, D. (2018). Ratiometric analysis using Raman spectroscopy as a powerful predictor of structural properties of fatty acids. *R. Soc. Open Sci.* 5:181483. doi: 10.1098/rsos.181483

Jan, A., Gokce, O., Luthi-Carter, R., and Lashuel, H. A. (2008). The ratio of monomeric to aggregated forms of Abeta40 and Abeta42 is an important determinant of amyloid-beta aggregation, fibrillogenesis, and toxicity. *J. Biol. Chem.* 283, 28176–28189. doi: 10.1074/jbc.M803159200

Jung, N., Moreth, T., Stelzer, E. H. K., Pampaloni, F., and Windbergs, M. (2021). Non-invasive analysis of pancreas organoids in synthetic hydrogels defines material-cell interactions and luminal composition. *Biomater. Sci.* 9, 5415–5426. doi: 10.1039/D1BM00597A

Kaji, S., Berghoff, S. A., Spieth, L., Schlaphoff, L., Sasmita, A. O., Vitale, S., et al. (2024). Apolipoprotein E aggregation in microglia initiates Alzheimer's disease pathology by seeding β-amyloidosis. *Immunity* 57, 2651–2668.e12. doi: 10.1016/j.immuni.2024.09.014

Kenigsbuch, M., Bost, P., Halevi, S., Chang, Y., Chen, S., Ma, Q., et al. (2022). A shared disease-associated oligodendrocyte signature among multiple CNS pathologies. *Nat. Neurosci.* 25, 876–886. doi: 10.1038/s41593-022-01104-7

Khatchadourian, A., Bourque, S. D., Richard, V. R., Titorenko, V. I., and Maysinger, D. (2012). Dynamics and regulation of lipid droplet formation in lipopolysaccharide (LPS)-stimulated microglia. *Biochim. Biophys. Acta* 1821, 607–617. doi: 10.1016/j.bbalip.2012.01.007

Kiraly, M., Foss, J. F., and Giordano, T. (2023). Neuroinflammation, its role in Alzheimer's disease and therapeutic Strategie. *J. Prev Alzheimers Dis.* 10, 686–698. doi: 10.14283/jpad.2023.109

Krafft, G. A., Jerecic, J., Siemers, E., and Cline, E. N. (2022). ACU193: an immunotherapeutic poised to test the amyloid β oligomer hypothesis of Alzheimer's disease. *Front. Neurosci.* 16:848215. doi: 10.3389/fnins.2022.848215

Kretschmer, A., Zhang, F., Somasekharan, S. P., Tse, C., Leachman, L., Gleave, A., et al. (2019). Stress-induced tunneling nanotubes support treatment adaptation in prostate cancer. *Sci. Rep.* 9:7826. doi: 10.1038/s41598-019-44346-5

Krishtal, J., Bragina, O., Metsla, K., Palumaa, P., and Tõugu, V. (2017). In situ fibrillizing amyloid-beta 1-42 induces neurite degeneration and apoptosis of differentiated SH-SY5Y cells. *PLoS One* 12:e0186636. doi: 10.1371/journal.pone.0186636

Kuhar, N., Sil, S., and Umapathy, S. (2021). Potential of Raman spectroscopic techniques to study proteins. *Spectrochim. Acta A* 258:119712. doi: 10.1016/j.saa.2021.119712

Kuperstein, I., Broersen, K., Benilova, I., Rozenski, J., Jonckheere, W., Debulpaep, M., et al. (2010). Neurotoxicity of Alzheimer's disease Aβ peptides is induced by small changes in the Aβ42 to Aβ40 ratio. *EMBO J.* 29, 3408–3420. doi: 10.1038/emboj.2010.211

Kwak, S. S., Washicosky, K. J., Brand, E., Maydell, D.Von, Aronson, J., Kim, S., et al. (2020). Amyloid-β42/40 ratio drives tau pathology in 3D human neural cell culture models of Alzheimer's disease. *Nat. Commun.* 11:1377. doi: 10.1038/s41467-020-15120-3

Lasch, P., and Noda, I. (2019). Two-dimensional correlation spectroscopy (2D-COS) for analysis of spatially resolved vibrational spectra. *J. Appl. Spectrosc.* 73, 359–379. doi: 10.1177/0003702818919880

Li, S., Jin, M., Koeglsperger, T., Shepardson, N. E., Shankar, G. M., and Selkoe, D. J. (2011). Soluble Aβ oligomers inhibit long-term potentiation through a mechanism involving excessive activation of extrasynaptic NR2B-containing NMDA receptors. *J. Neurosci.* 31, 6627–6638. doi: 10.1523/JNEUROSCI.0203-11.2011

Livak, K. J., and Schmittgen, T. D. (2001). Analysis of relative gene expression data using real-time quantitative PCR and the 2(-Delta Delta C(T)) method. *Methods* 25, 402–408. doi: 10.1006/meth.2001.1262

Loving, B. A., and Bruce, K. D. (2020). Lipid and lipoprotein metabolism in microglia. *Front. Physiol.* 11:393. doi: 10.3389/fphys.2020.00393

Mallesh, R., Juhee, K., Gharai, P. K., Gupta, V., Roy, R., and Ghosh, S. (2023). Controlling amyloid Beta peptide aggregation and toxicity by protease-stable ligands. *ACS Bio Med Chem Au* 3, 158–173. doi: 10.1021/acsbiomedchemau.2c00067

Manassero, G., Guglielmotto, M., Zamfir, R., Borghi, R., Colombo, L., Salmona, M., et al. (2016). Beta-amyloid 1-42 monomers, but not oligomers, produce PHF-like conformation of tau protein. *Aging Cell* 15, 914–923. doi: 10.1111/acel.12500

Matejka, N., and Reindl, J. (2019). Perspectives of cellular communication through tunneling nanotubes in cancer cells and the connection to radiation effects. *Radiat. Oncol.* 14:218. doi: 10.1186/s13014-019-1416-8

McCarthy, R. C., Lu, D.-Y., Alkhateeb, A., Gardeck, A. M., Lee, C.-H., and Wessling-Resnick, M. (2016). Characterization of a novel adult murine immortalized

microglial cell line and its activation by amyloid-beta. *J. Neuroinflammation* 13:21. doi: 10.1186/s12974-016-0484-z

Meijering, E., Jacob, M., Sarria, J.-C. F., Steiner, P., Hirling, H., and Unser, M. (2004). Design and validation of a tool for neurite tracing and analysis in fluorescence microscopy images. *Cytometry A* 58A, 167–176. doi: 10.1002/cyto.a.20022

Mensch, C., Konijnenberg, A., van Elzen, R., Lambeir, A.-M., Sobott, F., and Johannessen, C. (2017). Raman optical activity of human α -synuclein in intrinsically disordered, micelle-bound α -helical, molten globule and oligomeric β -sheet state. *J. Raman Spectrosc.* 48, 910–918. doi: 10.1002/jrs.5149

Meraz-Ríos, M. A., Toral-Rios, D., Franco-Bocanegra, D., Villeda-Hernández, J., and Campos-Peña, V. (2013). Inflammatory process in Alzheimer's disease. *Front. Integr. Neurosci.* 7:59. doi: 10.3389/fnint.2013.00059

Moreira, P. I., Carvalho, C., Zhu, X., Smith, M. A., and Perry, G. (2010). Mitochondrial dysfunction is a trigger of Alzheimer's disease pathophysiology. *Biochim. Biophys. Acta* 1802, 2–10. doi: 10.1016/j.bbadis.2009.10.006

Movasaghi, Z., Rehman, S., and Rehman, I. U. (2007). Raman spectroscopy of biological tissues. *Appl. Spectrosc. Rev.* 42, 493–541. doi: 10.1080/05704920701551530

Muñoz Herrera, O. M., and Zivkovic, A. M. (2022). Microglia and cholesterol handling: implications for Alzheimer's disease. *Biomedicines* 10:3105. doi: 10.3390/biomedicines10123105

Ortiz, C., Zhang, D., Xie, Y., Ribbe, A. E., and Ben-Amotz, D. (2006). Validation of the drop coating deposition Raman method for protein analysis. *Anal. Biochem.* 353, 157–166. doi: 10.1016/j.ab.2006.03.025

Pan, X., Zhu, Y., Lin, N., Zhang, J., Ye, Q., Huang, H., et al. (2011). Microglial phagocytosis induced by fibrillar β-amyloid is attenuated by oligomeric β-amyloid: implications for Alzheimer's disease. *Mol. Neurodegener.* 6:45. doi: 10.1186/1750-1326-6-45

Paris, D., Townsend, K., Quadros, A., Humphrey, J., Sun, J., Brem, S., et al. (2004). Inhibition of angiogenesis by Abeta peptides. *Angiogenesis* 7, 75–85. doi: 10.1023/B:AGEN.0000037335.17717.bf

Parodi-Rullán, R., Ghiso, J., Cabrera, E., Rostagno, A., and Fossati, S. (2020). Alzheimer's amyloid β heterogeneous species differentially affect brain endothelial cell viability, blood-brain barrier integrity, and angiogenesis. *Aging Cell* 19:e13258. doi: 10.1111/acel.13258

Peters, J., Park, E., Kalyanaraman, R., Luczak, A., and Ganesh, V. (2016). Protein secondary structure determination using drop coat deposition confocal Raman spectroscopy. *Spectroscopy* 31, 31–39.

Petratos, S., Li, Q.-X., George, A. J., Hou, X., Kerr, M. L., Unabia, S. E., et al. (2008). The beta-amyloid protein of Alzheimer's disease increases neuronal CRMP-2 phosphorylation by a rho-GTP mechanism. *Brain* 131, 90–108. doi: 10.1093/brain/awm260

Pezzotti, G. (2021). Raman spectroscopy in cell biology and microbiology. *J. Raman Spectrosc.* 52, 2348–2443. doi: 10.1002/jrs.6204

Qi, X., and Ma, J. (2017). The role of amyloid beta clearance in cerebral amyloid angiopathy: more potential therapeutic targets. *Transl. Neurodegener.* 6:22. doi: 10.1186/s40035-017-0091-7

Ralhan, I., Chang, C.-L., Lippincott-Schwartz, J., and Ioannou, M. S. (2021). Lipid droplets in the nervous system. *J. Cell Biol.* 220:2136. doi: 10.1083/jcb.202102136

Roberts, B. R., Lind, M., Wagen, A. Z., Rembach, A., Frugier, T., Li, Q.-X., et al. (2017). Biochemically-defined pools of amyloid-β in sporadic Alzheimer's disease: correlation with amyloid PET. *Brain* 140, 1486–1498. doi: 10.1093/brain/awx057

Russo, V., Candeloro, P., Malara, N., Perozziello, G., Iannone, M., Scicchitano, M., et al. (2019). Key role of cytochrome C for apoptosis detection using Raman microimaging in an animal model of brain ischemia with insulin treatment. *J. Appl. Spectrosc.* 73, 1208–1217. doi: 10.1177/0003702819858671

Rygula, A., Majzner, K., Marzec, K. M., Kaczor, A., Pilarczyk, M., and Baranska, M. (2013). Raman spectroscopy of proteins: a review. *J. Raman Spectrosc.* 44, 1061–1076. doi: 10.1002/jrs.4335

Sandberg, A., Berenjeno-Correa, E., Rodriguez, R. C., Axenhus, M., Weiss, S. S., Batenburg, K., et al. (2022). Aβ42 oligomer-specific antibody ALZ-201 reduces the neurotoxicity of Alzheimer's disease brain extracts. *Alzheimers Res. Ther.* 14:196. doi: 10.1186/s13195-022-01141-1

Sasmita, A. O., Depp, C., Nazarenko, T., Sun, T., Siems, S. B., Ong, E. C., et al. (2024). Oligodendrocytes produce amyloid-β and contribute to plaque formation alongside neurons in Alzheimer's disease model mice. *Nat. Neurosci.* 27, 1668–1674. doi: 10.1038/s41593-024-01730-3

Schindelin, J., Arganda-Carreras, I., Frise, E., Kaynig, V., Longair, M., Pietzsch, T., et al. (2012). Fiji: an open-source platform for biological-image analysis. *Nat. Methods* 9, 676–682. doi: 10.1038/nmeth.2019

Schützmann, M. P., Hasecke, F., Bachmann, S., Zielinski, M., Hänsch, S., Schröder, G. F., et al. (2021). Endo-lysosomal Aβ concentration and pH trigger formation of Aβ oligomers that potently induce tau missorting. *Nat. Commun.* 12:4634. doi: 10.1038/s41467-021-24900-4

Shipley, M. M., Mangold, C. A., and Szpara, M. L. (2016). Differentiation of the SH-SY5Y human neuroblastoma cell line. *J. Vis. Exp.* 108:53193. doi: 10.3791/53193

Sienski, G., Narayan, P., Bonner, J. M., Kory, N., Boland, S., Arczewska, A. A., et al. (2021). APOE4 disrupts intracellular lipid homeostasis in human iPSC-derived glia. *Sci. Transl. Med.* 13:4564. doi: 10.1126/scitranslmed.aaz4564

Singh, D. (2022). Astrocytic and microglial cells as the modulators of neuroinflammation in Alzheimer's disease. *J. Neuroinflammation* 19:206. doi: 10.1186/s12974-022-02565-0

Solis, E., Hascup, K. N., and Hascup, E. R. (2020). Alzheimer's disease: the link between amyloid-β and neurovascular dysfunction. *J. Alzheimers Dis.* 76, 1179–1198. doi: 10.3233/JAD-200473

Spangenberg, E., Severson, P. L., Hohsfield, L. A., Crapser, J., Zhang, J., Burton, E. A., et al. (2019). Sustained microglial depletion with CSF1R inhibitor impairs parenchymal plaque development in an Alzheimer's disease model. *Nat. Commun.* 10:3758. doi: 10.1038/s41467-019-11674-z

Stine, W. B., Jungbauer, L., Yu, C., and LaDu, M. J. (2011). Preparing synthetic Aβ in different aggregation states. *Methods Mol. Biol.* 670, 13–32. doi: 10.1007/978-1-60761-744-0_2

Tan, J. Z. A., and Gleeson, P. A. (2019). The role of membrane trafficking in the processing of amyloid precursor protein and production of amyloid peptides in Alzheimer's disease. *Biochim. Biophys. Acta Biomembr.* 1861, 697–712. doi: 10.1016/j.bbamem.2018.11.013

Tarawneh, R. (2023). Microvascular contributions to Alzheimer disease pathogenesis: is Alzheimer disease primarily an Endotheliopathy? *Biomol. Ther.* 13:830. doi: 10.3390/biom13050830

Targett, I. L., Crompton, L. A., Conway, M. E., and Craig, T. J. (2024). Differentiation of SH-SY5Y neuroblastoma cells using retinoic acid and BDNF: a model for neuronal and synaptic differentiation in neurodegeneration. *In Vitro Cell. Dev. Biol. Anim.* 60, 1058–1067. doi: 10.1007/s11626-024-00948-6

Thayanithy, V., O'Hare, P., Wong, P., Zhao, X., Steer, C. J., Subramanian, S., et al. (2017). A transwell assay that excludes exosomes for assessment of tunneling nanotube-mediated intercellular communication. *Cell Commun. Signal* 15:46. doi: 10.1186/s12964-017-0201-2

Thomas, R., Diaz, K., Koster, K. P., and Tai, L. M. (2017). In vitro assays to assess blood-brain barrier mesh-like vessel formation and disruption. *J. Vis. Exp.* 124:846. doi: 10.3791/55846

Ungureanu, A.-A., Benilova, I., Krylychkina, O., Braeken, D., Strooper, B.De, van Haesendonck, C., et al. (2016). Amyloid beta oligomers induce neuronal elasticity changes in age-dependent manner: a force spectroscopy study on living hippocampal neurons. *Sci. Rep.* 6:25841. doi: 10.1038/srep25841

Vadukul, D. M., Maina, M., Franklin, H., Nardecchia, A., Serpell, L. C., and Marshall, K. E. (2020). Internalisation and toxicity of amyloid-β 1-42 are influenced by its conformation and assembly state rather than size. *FEBS Lett.* 594, 3490–3503. doi: 10.1002/1873-3468.13919

Wang, X., and Gerdes, H.-H. (2015). Transfer of mitochondria via tunneling nanotubes rescues apoptotic PC12 cells. *Cell Death Differ.* 22, 1181–1191. doi: 10.1038/cdd.2014.211

Wendimu, M. Y., and Hooks, S. B. (2022). Microglia phenotypes in aging and neurodegenerative diseases. *Cells* 11:2091. doi: 10.3390/cells11132091

Winter, M. E. (1999). N-FINDR: an algorithm for fast autonomous spectral end-member determination in hyperspectral data. *Imaging Spectrom. V* 3753, 266–275. doi: 10.1117/12.366289

Yin, F. (2023). Lipid metabolism and Alzheimer's disease: clinical evidence, mechanistic link and therapeutic promise. *FEBS J.* 290, 1420–1453. doi: 10.1111/febs.16344

Yu, X., Hayden, E. Y., Xia, M., Liang, O., Cheah, L., Teplow, D. B., et al. (2018). Surface enhanced Raman spectroscopy distinguishes amyloid B-protein isoforms and conformational states. *Protein Sci.* 27, 1427–1438. doi: 10.1002/pro.3434

Zareba, J., and Peri, F. (2021). Microglial 'fat shaming' in development and disease. *Curr. Opin. Cell Biol.* 73, 105–109. doi: 10.1016/j.ceb.2021.07.007

Zhang, Y., Chen, H., Li, R., Sterling, K., and Song, W. (2023). Amyloid β-based therapy for Alzheimer's disease: challenges, successes and future. *Sig. Transduct. Target. Ther.* 8:248. doi: 10.1038/s41392-023-01484-7

Zhang, T., Song, C., Li, H., Zheng, Y., and Zhang, Y. (2022). Different extracellular β-amyloid (1-42) aggregates differentially impair neural cell adhesion and neurite outgrowth through differential induction of scaffold Palladin. *Biomol. Ther.* 12:1808. doi: 10.3390/biom12121808

Zhang, K., Sun, Z., Chen, X., Zhang, Y., Guo, A., and Zhang, Y. (2021). Intercellular transport of tau protein and β-amyloid mediated by tunneling nanotubes. *Am. J. Transl. Res.* 13, 12509–12522

Zhao, X., Zhang, S., Sanders, A. R., and Duan, J. (2023). Brain lipids and lipid droplet dysregulation in Alzheimer's disease and neuropsychiatric disorders. *Complex Psychiatry* 9, 154–171. doi: 10.1159/000535131

Zhu, S., Victoria, G. S., Marzo, L., Ghosh, R., and Zurzolo, C. (2015). Prion aggregates transfer through tunneling nanotubes in endocytic vesicles. *Prion* 9, 125–135. doi: 10.1080/19336896.2015.1025189

Zoltowska, K. M., Maesako, M., and Berezovska, O. (2016). Interrelationship between changes in the amyloid β 42/40 ratio and Presenilin 1 conformation. *Mol. Med.* 22, 329–337. doi: 10.2119/molmed.2016.00127

Glossary

Aβ	beta-amyloid
AD	Alzheimer's disease
AM II	amide II
APOE	apolipoprotein E
APP	Amyloid Precursor Protein
BBB	blood–brain barrier
BDNF	brain-derived neurotrophic factor
C	control
COX	cytochrome c oxidase
CXN	connection(s)
DCDRS	drop-coating deposition Raman spectroscopy
DNA	desoxyribonucleic acid
ELISA	Enzyme-linked-immunosorbent-assay
$FA\beta_{42}$	fibrillary amyloid-beta 1–42
FCS	fetal calf serum
IFN-γ	Interferon-gamma
IN	inflamed model
LPS	Lipopolysaccharide
$MA\beta_{42}$	monomeric amyloid-beta 1–42
mRNA	messenger ribonucleic acid
NMDA	N-methyl-D-aspartate
$OA\beta_{40}$	oligomeric amyloid-beta 1–40
$OA\beta_{1:3}$	oligomeric amyloid-beta 1–42 and 1–40 mixed 1:3
$OA\beta_{1:1}$	oligomeric amyloid-beta 1–42 and 1–40 mixed 1:1
$OA\beta_{3:1}$	oligomeric amyloid-beta 1–42 and 1–40 mixed 3:1
$OA\beta_{42}$	oligomeric amyloid-beta 1–42
PBS	phosphate buffered saline
PBS-T	phosphate buffered saline +0.05% Tween 20
PHE	phenylalanine
RNA	ribonucleic acid
RT-qPCR	Real-time quantitative polymerase chain reaction
SERS	surface-enhanced-Raman-spectroscopy
TEER	Transepithelial electrical resistance
THT	Thioflavin T
TNT	Tunneling nanotube
TYR	tyrosine